SYNTHESIS AND CHARACTERIZATION OF UNDOPED AND DOPED ZnO NANOPARTICLES PREPARED BY SOL-GEL PROCESS.

BY

ABDUB GUYO ALI

(B.Ed (Sc.), Hons.), K.U.

A dissertation presented in fulfilment of the requirements for the degree

MAGISTER SCIENTIAE

(MASTER OF SCIENCE)

In the

Faculty of Natural and Agricultural Sciences

Department of Physics

at the

University of the Free State, (Qwa Qwa Campus)

Republic of South Africa

Supervisor: Prof. B. F. Dejene

Co-supervisor: Prof. H. C. Swart

November 2009

Abstract

Nanotechnology is an emerging field of engineering that has intrigued a tremendous potential to change today's lives. Nanoparticles represent the transition region between individual atom/molecule and bulk materials have been attracting considerable research input, owing to some unique physical and chemical properties they exhibit. They are already being used in many applications. This is due to their potential useful size and shape dependant. They are provided with a number of quantum size effects that determine specific electro-physical performance. This is one of the reasons why the preparation and study of nanomaterials are important area of research. This work focuses on the synthesis and characterization of semiconducting metal oxides, the most widely used materials in powder and films forms. The aim is to compare the optical performances of zinc-oxides nanostructures obtained by means of sol-gel (SG) method. The microstructure quality (concentration and nature of defects) of materials which is a fundamental parameter to evaluate if the material is suitable for any applications are usually correlated with optical properties (intensity and spectral emission range) of materials. The idea of this work was to carry a basic characterization of the structural (by X-ray diffraction technique and scanning electron microscopy) and optical (photoluminescence measurements) properties of ZnO, ZnO in SiO_2 matrix and manganese doped ZnO nanoparticles samples prepared by sol-gel process. Initially, several samples of ZnO nanoparticles were successfully synthesised by varying the pH of the precursors. Secondly, manganese doped ZnO samples were synthesised by varying the concentration of manganese. The analysis of ZnO nanoparticles prepared under varying pH has displayed a dependence of structural quality, morphology as well as optical properties on the pH of the precursors. SEM images of manganese doped ZnO samples reveal nanorods of micrometer-size. XRD patterns confirm polycrystalline wurtzite structure of ZnO and particle sizes of about 7nm. High optical transmittance greater than 80% was achieved in the visible spectral wavelengths with UV-Vis optical absorption and transmission measurements. Photoluminescence spectra of the pure ZnO are composed of two main emission bands peaked at 388nm and 569nm. Both the blue (388nm) and the green (560nm) emissions in ZnO nanostructures were quenched,

although to different extent, when doped with Mn^{2+}. Mn-doped ZnO nanorods have several applications as the most suited materials for sensors, spintronics, better insulation materials etc.

Acknowledgements

I would like to give my sincere thanks and gratitude to:

My supervisor, Prof.B.F.Dejene, for his tireless and constant assistance, guidance and motivation.

My co-supervisor, Prof.H.C.Swart, for his advises, help, encouragement and patience.

Ms E .Coetsee and M.M .Biggs for measurements.

All members of staff and my fellow students at the Department of Physics, University of the Free State, for their valuable support and input.

National Research Foundation (NRF) for financial support.

#My family for their patience and understanding.

Most importantly, I thank GOD the ALMIGHTY; all my efforts would have been completely worthless without HIM.

Dedications

This work is dedicated to my son Guyo Abdub Guyo.

PHYSICS IS EASY, BUT PHYSICISTS ARE NOT.

TABLE OF CONTENTS

Chapter 1

1.1 INTRODUCTION

The unique and fascinating properties of group II-VI compound semiconductors have triggered tremendous motivation among the world scientists to study semiconducting nanoparticles. This is because it gives the opportunity to understand the physical properties in low dimensions and to explore their vast potential applications e.g. in optoelectronics. ZnO has featured as subject of thousands of research papers in the past 100 years, dating back as early as 1935 [1]. Valued for its ultra violet absorbance, wide chemistry, piezoelectricity and luminescence at high temperatures, ZnO has penetrated far into the industry, and is one of the critical building blocks in today's modern society [3]. More recently however, ZnO has entered the scientific spotlight for its semiconducting properties [4]. This latter in particular based on the large variations of the band gap and type of defect as a function of particle size and synthesis conditions respectively. Moreover, small nanoparticles allow the study of relevant surface properties due to the high surface to bulk ratio. In comparison with the bulk semiconductor, nanoparticles possess many special properties such as ultrafast optical nonlinear response, photo electricity switch and piezoelectric properties. Recently, the preparation of some semiconductor nanoparticles including CdSe, CdS and ZnS has been quite succesful [1-5]. In addition, their shapes and sizes can also be controlled. However, there has not been an equivalent success in the synthesis of metal oxides nanoparticles such as ZnO nanoparticles because of the complexity of hydrolyzation in metal ion. ZnO nanoparticles do not only have merits of ZnO semiconductor material such as a large exciton binding energy of 60meV and excellent stability, but also have novel characteristics of particularity of nanostructure. In semiconductor nanoparticles, strong confinement effect, appear when the size of the nanoparticles is comparable to the Bohr radius of the exciton in the bulk material. The confinement effect is obtained in ZnO when the particle sizes are equal or less than 0.7 Å. It is well known that small particles have the large surface-to-volume ratio and surface defects. The photoluminescence (PL) spectra of most ZnO nanoparticles samples showed a near-

band-edge (NBE) UV line accompanied by a strong visible luminescence, which can result in carrier/exciton lifetime and emission efficiency in the UV light devices. Zinc Oxide (ZnO) is a piezoelectric, dielectric transparent, semiconducting oxide, with a direct band of 3.37eV at room temperature and a large exciton binding energy (60meV), which is 2.4 times the effective thermal energy (K_{BT}=25meV) at room temperature, and bi-exciton energy is 15meV. This is one of the key parameters that ZnO exhibits near-UV emission, transparency, conductivity, and resistance to high temperature electronic degradation. In addition, ZnO is the hardest of the group II-VI semiconductors due to the higher melting point (2248K) and large cohesive energy (1.89eV) (therefore more resistant to wear), as well as one of the most piezoelectric semiconductors (d= 12.2×10-12C/N) with good piezoelectric coefficient (K_L=0.27) and its high adherence on various substrates [1-4]. There are also possible applications in micro electromechanical systems (MEMS), both in sensors, actuators and in the fabrication of acoustic and electro-optical devices. In particular, it can be used as Bulk Acoustic Wave (BAW) resonators and as thin Film Bulk Acoustic Wave (FBAR) Resonators or Surface Acoustic Wave (SAW) resonators [5]. It is commonly used as a catalyst, piezoelectric transducer, and photonic material. ZnO has several fundamental advantages over its chief competitor GaN and SiC. In fact, its free exciton is bound with 60 meV, much higher than that of GaN (21–25 meV); high energy radiation stability and amenability to wet chemical etching (although both are much better than Si or GaAs). Furthermore several experiments verified that ZnO is very resistive to high energy radiation, making it suitable candidate for space applications. It can be easily etched in all acids and alkalis. Due to this reason it can be used in the fabrication of small size devices e.g. transparent electrodes, window materials for displays and solar cells. Moreover it is used in a variety of technical applications, including porcelain enamels, heat resisting glass, an activator in vulcanization, an additive for rubber and plastics, pigment in paints with UV-protective and fungi static properties, spacecraft protective coatings, a constituent of cigarette filters, healing ointments, in optical waveguide, and many more [6]. ZnO has played an important role in the fabrication of transparent Thin Film Transistors (TFT), by depositing channel layer on a flexible substrate through low temperature processes, realizing transparent TFTs, and achieving extra functions such

as photo detections using ZnO channel. In this case the protective covering to prevent light exposure is eliminated since ZnO based transistors are insensitive to visible light. The deposited ZnO usually maintains a crystalline phase, although the deposition process is carried out even at room temperature [7, 8]. ZnO is a promising material for spintronics applications because of theoretical predictions of room temperature ferromagnetism, for example Curie temperature of > 300K for Mn-doped p-type ZnO and n-type doping in Fe-, Co-, or Ni- alloyed. ZnO have gained intense attention in the searching for high temperature dc Curie (T_c) ferromagnetic Diluted Magnetic Semiconductors (DMS) materials, which are based on ZnO. DMSs could exhibit ferromagnetism above room temperature upon doping with transition elements [3, 8]. ZnO crystallizes in three different crystal lattices. The first is the hexagonal wurtzite lattice which is mainly used in thin film industry as a transparent conducting oxide (TCO) or as a catalyst in methanol synthesis. The second is zinc blende form which can be stabilized by growing ZnO on substrates with cubic lattice structure. In both cases, the zinc and oxide are tetrahedral. The third structure is more known to geologist as the rock salt NaCl-type structure (only observed at high pressure) and is a spinal phase that is used in the understanding of the earth's lower mantle. But a thermodynamically stable phase is the wurtize structure, which is well known to show piezoelectric properties with a large electromechanically coupling factor and a low dielectric constant $\varepsilon(0) = 8.75$ to $\varepsilon(\infty) = 3.75$.

1.2 Motivation and aim of the work

The aim of this work is to reveal specific properties of ZnO nanocrystalline materials prepared by Sol-Gel technique. Initially series of undoped ZnO samples were prepared by sol-gel technique. Later Mn-doped ZnO samples were synthesis by addition of concentrations of do-pants and annealed at different temperatures. The various preparation processes should result in different surface morphology, structural and micro structural properties of the nanostructures. Also the optical properties of ZnO are known to be sensitive for its structural quality.

The main objectives are:

- Characterization of structural, micro structural and photoluminescence properties of obtained material.
- Investigate effect of pH on the structural, micro structural and photoluminescence properties of the powder samples.
- Study the effects of dopant (Mn^{2+}) on the structural, micro structural and photoluminescence properties of the samples.
- Correlation between the main technological parameters and material properties.

The microstructure of ZnO nanostructures strongly depend on the pH. In order to investigate this hypothesis, series of sample with varying pH was prepared. Herein, is a report on a simple sol-gel method in ethanol solution to prepare ZnO nanoparticles, SiO_2:Ce^{3+} and ZnO: SiO_2:Ce^{3+} composites. The influence of the NaOH concentration on structural and optical properties of the as-prepared pure ZnO nanoparticles and the corresponding effect of the ZnO nanoparticles in a SiO_2 matrix doped with Ce^{3+} (0.5 mol %) were investigated. The structure, microstructure and optical emitting properties of such nanosized heterostructures are of great interest for optoelectronic applications in terms of present nanotechnologic trend. In order to investigate the possibility of obtaining the low-sized ZnO structures by sol-gel technique, we have examined three categories of samples of pure ZnO, ZnO:SiO_2 and ZnO:SiO_2:Ce^{3+}.

A third motivation of this study is to reveal the effect of dopants on the properties of zinc oxide. ZnO is always deviated from stoichiometry and present intrinsic defects such as Zn-rich or O-deficient atmosphere. The ability to find the way to engineer the band gap of ZnO by doping is a great challenge. For that purpose the samples of ZnO as-prepared and doped will be investigated.

1.3 Significance of the study

The aim of this project is to synthesize zinc oxide (ZnO) nanoparticles by Sol-gel process. The investigation reported on this thesis was carried out in three stages. The effect of pH on the structural and optical properties of ZnO nanoparticles was initially investigated. This was done by preparing ZnO powder by using different molar concentration of NaOH, while keeping all other factors constants. In the second stage,

ZnO nanoparticles prepared previously was added to $SiO_2:Ce^{3+}$ matrix to study the energy transfer by ZnO to $SiO_2:Ce^{3+}$ matrix. Thirdly, in order to engineer the band gap ZnO was doped with Mn^{2+} and the effect was also studied. The prepared nanoparticles were characterized by using different techniques.

1.4 Thesis Layout

This thesis is organized into seven chapters. Chapter one is the general introduction of the thesis. In chapter two, an overview of ZnO properties is given and different methods of the synthesis of metallic nanoparticles are outlined. The experimental procedures followed during preparation of ZnO nanoparticles and characterization techniques discussed in detailed in chapter three; some description and operation of characterization methods are included. The experimental results and parameters on ultimate effect of pH on ZnO nanoparticles quality are presented and discussed in chapter four. Chapter five describes the energy transfer by ZnO to $SiO_2:Ce^{3+}$ matrix. Effect of doping ZnO with mn^{2+} is described in chapter six. The seventh chapter gives the conclusion and possible future work in this area.

References

[1] C. W. Bunn, "The lattice-dimensions of zinc oxide," Proc. Phys. Soc.London 47:835, 1935.

[2] H. L. William, "Synthesis and characterization of ZnO for piezoelectric applications", PhD thesis, School of materials science & engineering, Georgia Institute of Technology USA. (2006)

[3] Ü. Özgür, Ya. I. Alivov, C. Liu, A. Teke, M. A. Reshchikov, S. Doğan, V. Avrutin, S.J. Cho and H. Morkoçd, Journal of Applied Physics **98**,041301(2005)

[4] J. Chumming, "Growth and characterization of ZnO and ZnO-based Alloys-$Mg_xZn_{1-x}O$ and $Mn_xZn_{1-x}O$" PhD thesis, Department of materials science and Engineering, North Carolina state university, Raleigh. (2003)

[5] G. Ferblantier, F. Mailly, R. Al Asmar, A. Foucaran, F. Pascal-Delannoy, sensor and actuators A **122** 184-188 (2005)

[6] S. J. Pearton, D. P. Norton, K. Ip, Y.W. Heo, T. Steinerb, Super lattices and Microstructures **34** 29–32 (2003)

[7] H. Günter "The characterization of bulk as-grown and annealed ZnO by Hall effect" PhD thesis, University of Pretoria, Pretoria

[8] I. Ivanov and J. Pollmann, Phys. Rev. B **24**. 7273-7276 (1981).

[9] W. Göpel, J. Pollmann, I. Ivanov and B. Reihl, Phys. Rev. B **26** (1982) 3144-3150.

[10] N. Izyumskaya, V. Avrutin, Ü. Özgür, Y. I. Alivov, and H. Morkoç phys. stat. sol. **244**, No. 5, 1439–1450 (2007)

[11] Y. Ryu, T. S. Lee, J. A. Suburban, H. W. White, Bong-Jin Kim, Yoon-Soo Park, and Chang-Joo Youn, Appl. Phys. Lett. **88**, 241108 (2006).

[12] L. Stolt, J. Hedstrom, M. Ruckh, K. V. Velthaus, and H. W. Schcok, Appl. Phys. Letter, **62**, 597, (1993).

[13] T. Olorunyolemi, A. Birnboim, Y. Carmel, O. C. Wilson, Jr., and I. K. Lloyd, J. Am. Ceram. Soc. **85**, 1249 (2002).

[14] D. I. Florescu, L. G. Mourokh, F. H. Pollak, D. C. Look, G. Cantwell, X. Li, J. Appl. Phys. **91**, 890 (2002).

[15] D. C. Look, J. W. Hemsky, J. R. Sizelove, Phys. Rev. letters Vol. **82**, No. 12 (1999).

[16] J. Chennupati and P .Stephen J. "Zinc Oxide Bulk, Thin films and Nanostructures" 1st edition (2006).

Chapter 2

Fundamental properties of ZnO

2.1 Crystal structure

Structurally, ZnO has a non-centrosymmetric wurtzite crystal structure with polar surfaces. The wurtzite structure of ZnO can be considered to be composed of two interpenetrating hexagonal close packed (hcp) sub lattices of cation (Zn) and anion (O) displaced by the length of cation-anion bond in the c-direction. The lattice constant of the ZnO hexagonal unit cell are a = 3.2500Å and c = 5.2060Å. Since ZnO is a two-element compound with different atoms, so c/a ratio for ZnO hcp unit is 1.60, which is a little smaller than the ideal value of 1.633 of hcp. Each hexagonal close packed (hcp) consists of one type of atom displaced with respect to each other along the threefold c-axis by the amount of u = 3/8 = 0.375 (in an ideal wurtzite structure) in fractional coordinates (the u parameter is defined as the length of the bond parallel to the c axis, in units of c or nearest neighbor distance b divided c) [1]. α and β are the bond angle 109.070 (in an ideal wurtzite crystal) as shown in Figure 2.1. Schematic representation of a wurtzitic ZnO structure [2]. Each sub lattice includes four atoms per unit cell and every atom of one kind (group II atom) is surrounded by four atoms of the other kind (group VI), or vice versa, which are coordinated at the edges of a tetrahedron. In a real ZnO crystal, the wurtzite structure deviates from the ideal arrangement, by changing the c/a ratio or the u value. The deviation from that of the ideal wurtzite crystal is probably due to lattice stability and ionicity. The point defects such as zinc antisites, oxygen vacancies, and extended defects, such as threading dislocations also increase the lattice constant in ZnO crystal, but for a small extent in heteroepitaxial layers. There exists a strong relationship between the c/a ratio and the u parameter in that when the c/a ratio decreases, the u parameter increases in such a way that those four tetrahedral distances remain nearly constant through a distortion of tetrahedral angles due to long-range polar interactions. These two slightly different bond lengths will be equal if the following relation holds:

$$\mu = \frac{1}{2}(\frac{a2}{c2}) + \frac{1}{4}$$

Where, a and c are lattice parameters.

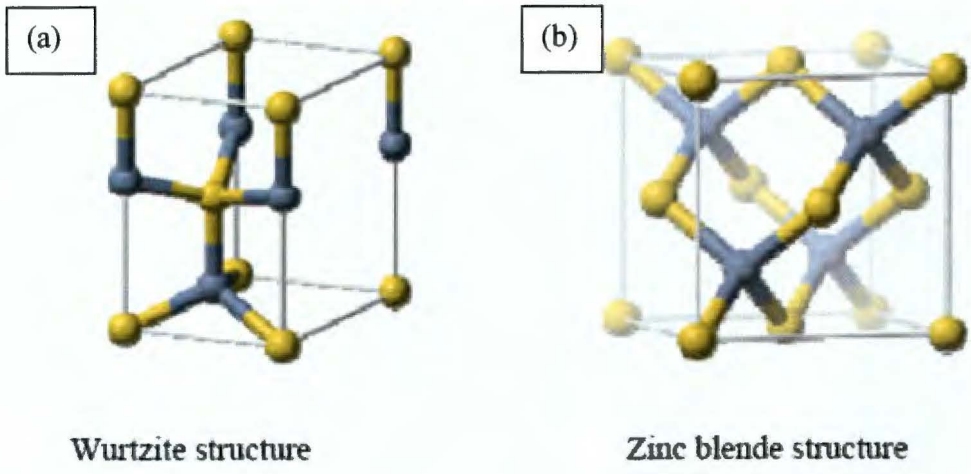

Figure 2.1(a) Wurtzite and (b) Zinc blende structure unit cell. The blue balls represent oxygen atoms, and each yellow ball represents either a zinc atom or an iron atom.

The tetrahedral coordinated diamond, zinc blend, and wurtzite-type crystal structures have the quality for covalent chemical binding with sp3 hybridization. While the Group IV element semiconductors like diamond, silicon and germanium have completely covalent bonding, one has an increasing admixture of ionic binding when going from the Group IV over the III–V and II–VII to the I–VII semiconductors, ending with completely ionic binding for the II–VI and I–VII insulators like MgO or NaCl, which frequently crystalline in the rock salt structure. ZnO already has a substantial ionic bonding component, as shown in the "historic" diagram of Figure 2 .1(b), which shows ZnO in the "centre of solid state physics". Because of this small portion of ionic binding, the bottom of the conduction band, or the lowest unoccupied orbital (LUMO), is formed essentially from the 4s levels of Zn^{2+} and the top of the valence band, or highest occupied molecular orbital (HOMO), from the 2p levels of O^{2-}. The band gap between the conduction and valence bands is about 3.37 eV at room temperature.

2.2 Lattice Parameters

Lattice parameters are considered important when one has to develop semiconductors devices. There are mainly four factors which affect the lattice parameters of semiconductors;

- Free-electron concentration which affects the potential of the bottom of conduction band normally occupied by electrons.
- Concentration of impurities and defects and the difference in ionic radii between these defects and impurities with respect to substituted matrix ions.
- External strains (for example, those induced by substrate).
- Temperature.

On the other hand, the strict periodicity of the lattice is disturbed by many imperfections or defects. These imperfections or defects have a considerable, controlling influence on mechanical, thermal, electrical and optical properties of semiconductors. They determine the plasticity, hardness, thermal and electrical conductivities. Commonly the lattice parameters of any crystalline materials are measured accurately by high-resolution X-ray diffraction (HRXRD). Table 2.1 shows a comparison of measured and calculated lattice parameters of ZnO, c/a ratio and u parameters reported by several groups [1, 8].

Table 2.1: Measured and calculated lattice constants and u parameters of ZnO, (a) measured by using X-ray diffraction, (b) measured by using powder X-ray diffraction and (c) calculated by using ab-initio periodic linear combination of atomic orbital (LCAO) method.

	a (Å)	c(Å)	c/a	u
(a)	3.2496	5.2042	1.6018	0.3819
(b)	3.2501	5.2071	1.6021	0.3817
(c)	3.286	5.241	1.595	0.383

2.3 Electronic band structure

A very important property of any given semiconductor is its band structure, because many important properties such as the band gap and effective electron and hole masses are derived from it. ZnO is considered most suitable semiconductor among all its family members for ultraviolet lasing at room temperature, device application as well as possibilities to engineer the band gap, for this reason a clear understanding of the band structure is important to explain the electrical properties and many other phenomena because it determines the relationship between the energy and the momentum of the carriers. Experimental methods to determine band structures normally involve measurements by UV and X-ray reflection/absorption/emission techniques as well as photoelectron spectroscopy (PES) and angular resolved photoelectron spectroscopy (ARPES) has been used to measure the electronic core levels in solids. These methods basically measure the energy difference by inducing transitions between different electronic levels (for example, transitions from the upper valence-band states to the upper conduction states, and the lower valence-band states) [2, 8, 12]. Angular resolved photoelectron spectroscopy (ARPES) along with synchrotron radiation excitation has been recognized as a powerful tool that enables experimental bulk and surface electronic band structure determination under the assumption of k conservation and singly nearly free electron like final band. The other important method for the analysis of the energy region is based on photoelectric effect extended to X-ray region, namely, photoelectron spectroscopy (PES). The peaks emission spectrum corresponds to electron emission from the core levels without inelastic scattering which is usually accompanied by a far-less-intense tail region in the spectrum. The most important aspect of the band structure of ZnO is that it has a direct band gap. Recently the band structure was calculated using an empirical tight-binding Hamiltonian. The band structure E (k) for ZnO is given along some symmetry line in the Brillion zone. Important thing is to know about band gap between the occupied and empty band (represented by Γ_1 and $\Gamma_{1.5}$.). Optical band gap (E_g) of ZnO is about 3.3 eV. Actually this is the energy difference between full and empty state. These filled states are called the valence band, and empty at the top of the valence band is usually zero

energy and is called valence band edge. The empty states above the gap are called the conduction band. The lowest point in the conduction band is called the conduction band edge. For ZnO the conduction band edge is at k=0, the Γ point, which is also the k-value of the valence band edge. Since for ZnO the valence band and the conduction band edges occur at the same k-values, the material is called a direct band gap semiconductor [13, 14]. From the band gap structure (fig.2.2) six valence bands can be between -6eV and 0eV. These six valence bands correspond to the oxygen's 2p orbital that contribute to the band structure.

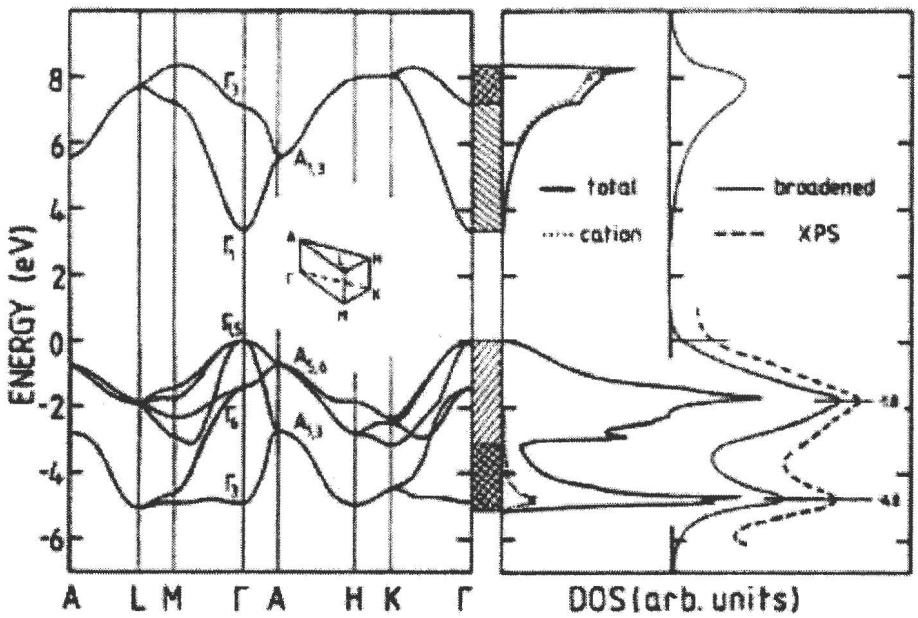

Figure 2.2 Band structures of ZnO, the zero in the graphs is taken as the valence band upper edge [14].

Below - 6 eV at about - 20 eV the valence band terminates with the oxygen's 2s core like state. For the conduction band there are two bands visible (above 3eV). These bands are strongly localized on the Zn and correspond to the unoccupied Zn: 3s levels.

2.3.1 Band gap engineering

In order to make progress in modern devices, like ZnO UV detectors and field transistors (FET), modulation of the band gap is required. It has been verified due to the development of $Mg_xZn_{1-x}O$ and $Be_xZn_{1-x}O$ alloys for larger band gap materials and $Cd_yZn_{1-y}O$ alloys for smaller band gap materials, allowing band gap tuning in a wide range. The energy gap $E_g(x)$ of a ternary semiconductor $A_xZn_{1-x}O$ (where A = Mg, Be or Cd) is determined by the following empirical equation;

$$E_g(x) = (1-x)E_{ZnO} + xE_{AO} - b(x)(1-x) \tag{2.2}$$

Where b is the bowing parameter and E_{AO} and E_{ZnO} are the band gap energies of compounds AO (MgO, CdO, and BeO) and ZnO, respectively. The bowing parameter depends on the difference in the electro negativities of the end binaries ZnO and AO. The band gap vs. the in-plane lattice is constant for all ternaries, namely $Be_zZn_{1-z}O$, $Mg_xZn_{1-x}O$ and $Cd_yZn_{1-y}O$ is shown in figure 2.3. Mg_xZn_{1-x} alloys are considered as a suitable material for barrier layers in ZnO/ (Mg, Zn)O super lattice structures. Because alloying ZnO with MgO (E_g = 7.7eV) enables widen the band gap of ZnO with very little change in the lattice constants.

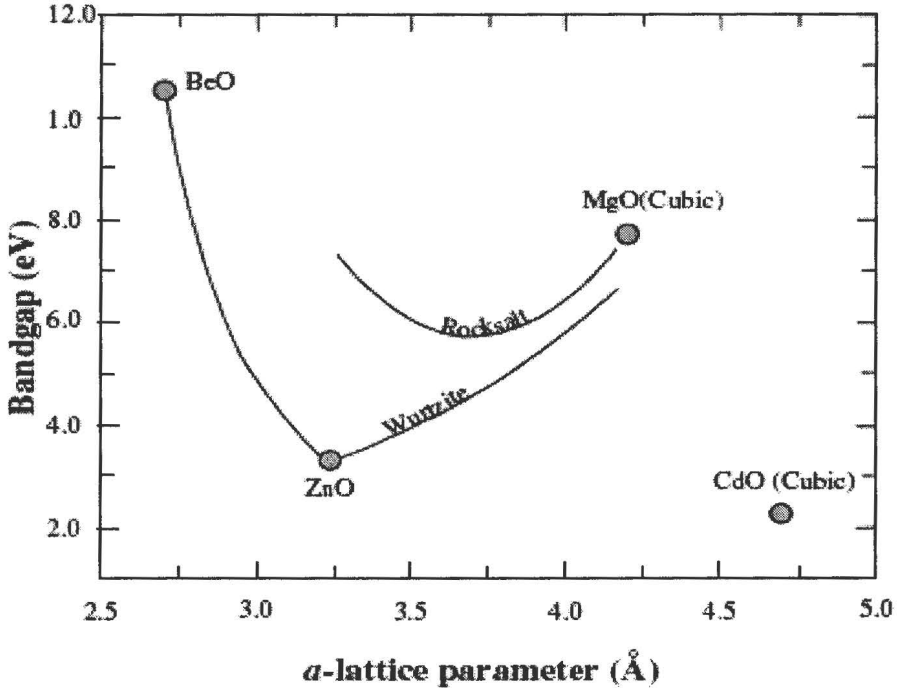

Figure 2.3 Band gap vs. in-plane lattice constants for the ternaries of ZnO, namely, $Be_zZn_{1-z,}O$, $Mg_xZn_{1-x}O$ and $Cd_yZn_{1-y}O$ [15].

ZnO has a wurtzite structure (a = 3.24 L and c = 5.20 L) while MgO has a cubic structure (a = 4.24 L). $Mg_xZn_{1-x}O$ with composition up to near 40% and band gap near 4eV remains wurtzitic, but after the composition of near about 60% their structures become cubic. In the intermediate region the quality of the films is not good due to conversion of different mixed polytypes are present in it. Substitution of Be for Zn increases the band gap of ZnO. Unlike MgZnO, which changes over to the cubic form beyond the 40% Mg concentration, $Be_zZn_{1-z}O$ is wurtzitic throughout the entire compositional range as the equilibrium state of BeO is wurtzitic. For narrower band gaps, which are desirable for wavelength tenability and attaining band gap corresponding to the visible spectrum, $Cd_yZn_{1-y}O$ alloy would be a good candidate because of the small direct band gap of CdO (2.3eV). There has not been as much progress with Cd doped ZnO. We should mention that CdO is cubic also and large

concentrations of Cd in ZnO lattice would cause behaviour similar to the MgZnO case in the intermediate region [15, 16].

2.4 Properties of wurtzite ZnO

Table 2.2 shows a compilation of the basic physical parameters for ZnO. Still some uncertainty exists in these values. For example, in few reports, only the physical properties of p-type ZnO has been mentioned and therefore the hole mobility and effective mass are still in debates [10, 11].

Table 2.2 Basic physical parameters for ZnO.

Property	Values
Lattice parameters at 300 K	
a_0	3.2495Å
c_0	5.2069Å
a_0/c_0	1.602 (ideal hexagonal structure shows 1.633)
u	0.345
Density	5.606 g cm^{-3}
Stable phase at 300 K	Wurtzite
Bond length	1.977μm
Melting point	1975 ◦C
Thermal conductivity	0.6, 1–1.2
Linear expansion coefficient (/C)	a_0: 6.5 × 10^{-6} , C_o :3.9x10^{-6}
Static dielectric constant	8.656
Refractive index	2.008, 2.029
Energy gap	3.4 eV, direct

Intrinsic carrier concentration	$<106\ cm^{-3}$
Breakdown voltage (10^{6} V cm^{-1})	5.0
Saturation velocity (10^{7} cms^{-1})	3.0
Exciton binding energy	60 meV
Electron effective mass	0.24
Electron Hall mobility at 300 K for low n-type conductivity	200 cm^{2} V−1 s^{-1}
Hole effective mass	0.59
Hole Hall mobility at 300 K for low p-type conductivity	5–50 cm^{2} V−1 s^{-1}
Knoop hardness	0.5N/cm^{2}
Minimum pressure at melting point	7.82atm
Ionicity	62%
Heat capacity Cp	9.6 cal/molK
Heat of crystallization ΔHls	62KJ/mol
Young's modulus E (bulk ZnO)	111.2±4.7 GPa
Bulk modulus, B (Polycrystalline ZnO)	142.2 Gpa
dB/dP	3.6
Spontaneous polarization (C/m^{2})	-0.057
Born effective charge*	2.10

2.4.1 Optical properties

The optical properties of a semiconductor are associated with both intrinsic and extrinsic deffects. Intrinsic optical transitions take place between the electrons in the conduction band and holes in the valence band, including excitonic effects due Coulomb's interactions. The main condition for excitonic formation is that the group velocity of the electrons and holes is equal. Excitons are classified into free and bound excitons. In high quality samples with low impurity concentrations the free excitons can also exhibit

excited states, in addition to their ground-state transitions. Extrinsic properties are related to dopant or defects, which usually create discrete electronic states in the band gap, and therefore influence both optical-absorption and emission process. As we mentioned above, ZnO is a direct band semiconductor and a transparent conductive material. ZnO films are transparent in the wavelength range of 0.3 and 2.5 micrometer, and plasma edges lies between 2 and 4 micrometer depending on the carrier concentration. It is well known that a shift in the band gap edge appears with an increase in carrier concentration. This shift is known as Burstein-Moss shift. Optical transition in ZnO have been studied by a variety of experimental techniques such as optical absorption, transmission, reflection, photo reflection, spectroscopic ellipsometry, photoluminescence, cathode luminescence calorimetric spectroscopy etc. Room temperature PL spectrum of ZnO is usually composed of a near UV- emission band (375nm) and a green emission band (510nm) although a yellow-orange band (610nm) can also be observed in some situations. The near UV-band is closely related to the excitonic nature of the material and maybe superposed will be free exciton emission its phonon replica, bound exciton emission, as well as biexciton emission. The observation of luminescence from exciton is usually difficult even at low temperature. This comes from a lot of factors [17]. First the efficiency of radiative emission is low even for direct band gap semiconductors, which is often found to be 10^{-1} to $10^{-3.}$ A large part of the radiative emission comes from bound-excitation complexes and defect centers. Exciton emission is limited by the internal reflection of the exciton and the small escape length. As quasi-particle, exciton moves with their group velocity through the semiconductor. During this movement, exciton can be trapped or scattered by impurities and phonons. When it eventually reaches the surface of the semiconductor, in most cases, it will be reflected back into the semiconductor. Except the internal reflection, the radiative combination yield from free-exciton is also limited by the small escape length, which defined as the depth from which exciton can reach the surface. Only the free-exciton inside the escape length can have the contribution to the luminescence.

The research interest for the green band emission in ZnO can be traced back to the early stage of last century. Due to this green emission, ZnO is considered as an important luminescence material for the planar display and short-decay

cathodoluminescence screens. Unfortunately, the mechanisms behind this emission band are still unclear even though the researches on this topic have been lasted for many years. Green band emission was first attributed to an excess of Zn ions. Almost all the proposed mechanisms about the green emission are attributed to the native lattice defects except the one that is based on the divalent Cu impurities. In the order of time evolution, these models can be listed as follows [18];

(a) Zn-excess related transitions (Zn^{+} to Zn^{2+});

(b) Oxygen vacancies (V_o);

(c) Transitions at Cu^{2+};

(d) Zn interstitial to Zn vacancy (Z_{in} to V_{zn});

(e) Singly ionized oxygen vacancies (transition from V_o^{+} to VB);

(f) Transitions from shallow traps to doubly-ionized oxygen vacancies (V_o^{++});

(g) DA pair (V_o^{+} to V_{zn}).

2.4.2 Thermal Properties

Thermal expansion coefficient (TEC)

The change in temperature affects the lattice parameters of semiconductors. Thermal expansion coefficient, are defined as $\Delta a/a$ *or* α_a and$\Delta c/c$ or α_c for in and out of plane cases, respectively. The stoichiometry, presence of extended defects and free carrier concentration also affect the thermal expansion coefficient. The X-ray powder diffraction method developed by Reeber was used to measure the temperature dependence of lattice parameters of ZnO as shown in Figure 2.5. Lattice parameters of ZnO were measured over the temperature range 4.2 -299 K, fourth-order polynomials were fitted using the least-squares method, which gives the minimum for the a_0 parameter at 93 K. The c_o parameter has much uncertainty, did not give any minimum value, perhaps due to its less precision and uncertainty in measurement [19].

Thermal conductivity

Thermal conductivity (k), having a kinetic nature, is determined by vibration, rotation and electronic degree of freedom. It is really important property of semiconductors when these materials are used in high-power, high-temperature or optoelectronic devices. The electronic thermal conductivity is very small, having light carrier concentration, which is negligible. For high pure crystals, phonon-phonon scattering is ideally proportional to T^{-1} at the temperatures higher than the Debye temperature. Point defects, such as vacancies, impurities and isotope fluctuations in a ZnO affect the thermal conductivity of ZnO material.

2.4.3 Electrical Properties

As a direct and wide band gap semiconductor with a large exciton binding energy (60meV), ZnO is representing a lot of attraction for optoelectronic and electronic devices. For example, a device made by material with a larger band gap may have a high breakdown voltage, lower noise generation, and can operate at higher temperatures with high power operation. The performance of electron transport in semiconductor is different at low and high electric field. At sufficient low electric fields, the energy distribution of electrons in ZnO is unaffected much, because the electrons can't get much energy from the applied electrical field, as compared with their thermal energy. So the electron mobility will be constant because the scattering rate, which determines the electron mobility, doesn't change much. When the electrical field is increased, the energy of the electrons from the applied electrical field is equivalent to the thermal energy of the electron. The electron distribution function changes significantly from its equilibrium value. These electrons become hot electrons, whose temperature is higher than the lattice temperature. So there is no energy loss to the lattice during a short and critical time. When the electron drift velocity is higher than its steady-state value, it is possible to make a higher frequency device.

2.5 Doping and defects in ZnO

In recent years, much attention has been focused on wide band gap semiconductors materials because of their excellent potential for blue light emitting devices, short-wavelength laser diodes and detectors in UV-blue spectral region. As wide band gap ZnO is gaining much importance for the possible application due to the capability of ultraviolet lasing at room temperature and possibilities to engineer the band gap. In order to attain the potential offered by ZnO, both high-quality n-and p-type ZnO are essential. But it is very difficult to obtain the bipolar carrier doping (both n and p types) in wide-band-gap semiconductors such as GaN and II-VI compound semiconductors including ZnS, ZnSe, and ZnTe. Unipolar doping has not been a surprising issue in wide-band-gap semiconductors. ZnO, GaN, ZnS, and ZnSe are easily doped to n-type, while p-type doping is difficult. All undoped ZnO to date has been found to be n-type, with donor concentrations typically around 10^{17} cm^{-3} for present-day, high-quality material, but sometimes as high as 10^{21} cm^{-3}, for highly doped material. The situation is opposite for ZnTe where p-type doping is easily obtained, while n-type doping is difficult. The main characterization techniques used to find the shallow electrical defects in semiconductor materials are photoluminescence and temperature dependent Hall Effect measurements. Figure 2.4: summarizes the main defect types that can occur in single crystal ZnO, although all of them are not shallow defects. Zn_i and V_{zn} are the zinc interstitial and zinc vacancy respectively while O_i and V_o denote the oxygen interstitial and vacancy respectively. Impurity atom X can occur either as interstitials X_i or substitutionals X_{zn} and X_o on zinc and oxygen sites respectively. D and A denote that the relevant impurity is expected to be donor or acceptor respectively. X does not have to be a foreign atom. A Zn-on-O antisite can for example also occur.

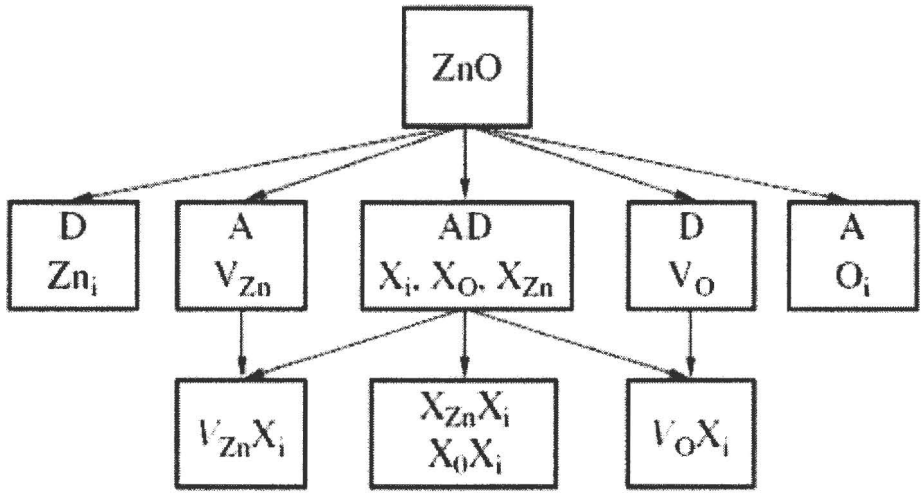

Figure 2.4: Summary of defect types that may occur in ZnO [20]

N-type doping

ZnO has wurtzite structure, excess zinc is always found in ZnO. Due to this zinc excess, ZnO is a non-stoichiometric compound and n-type semiconductor. Undoped ZnO shows intrinsic n-type conductivity with high electron densities of about 10^{21} cm^{-3}. Zinc interstitials Zn_i and the oxygen vacancy V_O are known to be the dominant native donor in unintentionally ZnO film, but still it is debatable issue. Photoluminescence and temperature dependent Hall studies of electron irradiated ZnO have shown that Zn_i is the most likely candidate for purely lattice-related dominant shallow donor, with an activation energy about 30-50 meV. It has been argued that the n-type conductivity of unintentionally doped ZnO film is only due to hydrogen (H), which is treated as a shallow donor with activation energy of 31 meV instead of Zn_i. This assumption is valid because hydrogen (H) is always present in all growth methods and can easily diffuse into ZnO in large amounts due to it large mobility [20]. Hydrogen has been considered as a shallow donor candidate, much research has been done on hydrogen (H) in ZnO. During seeded chemical vapor transport (SCVT) growth of ZnO, it has been shown that hydrogen with activation energy 39 meV acts as main donor. This donor disappears

through on annealing process. [12, 20]. N-type doping of ZnO is relatively easy as compared to p-type doping. Group III elements Al, Ga and In as substitutional elements for Zn and group-VII elements Cl and I as substitutional elements for O can be used as n-type dopants. Doping with Al, Ga and In has been attempted by many groups, resulting in high-quality, highly conductive n-type ZnO films. Al-doped ZnO films were grown by MOCVD. The films obtained through this method are high by conductivity with minimum resistivity as compared to Ga-doped ZnO films prepared by Chemical-vapour deposition [2, 12].

P-type doping

It is very difficult to obtain p-type doping in wide band gap semiconductors. Acceptors in ZnO can also take place from both lattice defects and impurity atoms. The oxygen interstitial O_i and zinc vacancy V_{Zn} are both known to be acceptors in ZnO. Deep impurity level can also be source of doping problem, causing large resistance to the formation of shallow acceptor level.

P-type doping in ZnO may be possible by substituting either group-I elements (Li, Na, and K) for Zn sites acting as shallow acceptors and group-V elements (N, P, and As) are found to act as deep acceptors on O sites. It was shown that group-I elements could be better p-type dopants than group-V elements in terms of shallowness of acceptor levels. However, group-I elements tend to occupy the interstitial sites, due to their small atomic radii, rather than substitutional sites, and therefore, they act as donors instead of acceptors. Moreover, significantly larger bond length for Na and K than ideal Zn–O bond length (1.93 Å) induces lattice strain, increasingly forming native defects such as vacancies which compensate the shallow dopants. These are among the many causes leading to difficulties in attaining P-type doping in ZnO [18, 19]. Group V elements (N, P, As) except N, both P and As, have a larger bonds lengths. That's why they are likely to form antisites to avoid the lattice strain. Unfortunately for p-conduction these elements have a tendency towards antisite formation, i.e. they can substitute not only oxygen but also zinc atoms, in which case they act as donors. Nitrogen (N) appears to be good

candidate for a shallow P-type dopant in ZnO with smallest ionization energy, although N is not soluble in ZnO, and doping can be achieved by ion implantation [2, 12, 20,].

References

[1] Ü. Özgür Ya, I. Alivov, C. Liu, A. Teke, M. A. Reshchikov, S. Doğan, V. Avrutin, S.J. Cho and H. Morkoçd, journal of applied physics **98**,041301(2005)

[2] A. Luis Manuel "Silva Study of structural, electrical, optical and magnetic properties of ZnO based films produced by magnetron sputtering" PhD thesis, University of Puerto Rico UPR.(2006)

[3] S. J. Pearton, D. P. Norton, K. Ip, Y.W. Heo, T. Steinerb, Super lattices and Microstructures **34** 29–32 (2003)

[4] www.semiconducators.co.uk

[5] H. Günter "The characterization of bulk as-grown and annealed ZnO by Hall effect" PhD thesis, University of Pretoria, Pretoria

[6] I. Ivanov and J. Pollmann, Phys. Rev. B **24**. 7273-7276 (1981).

[7] W. Göpel, J. Pollmann, I. Ivanov and B. Reihl, Phys. Rev. B **26** (1982) 3144-3150.

[8] N. Izyumskaya, V. Avrutin, Ü. Özgür, Y. I. Alivov, and H. Morkoç phys. stat. sol. **244**, No. 5, 1439–1450 (2007)

[9] Y. Ryu, Tae-Seok. Lee, J. A. Lubguban, H. W. White, Bong-Jin Kim, Yoon-Soo Park, and Chang-Joo Youn, Appl. Phys. Lett. **88**, 241108 (2006).

[10] L. Stolt, J. Hedstrom, M. Ruckh, K. V. Velthaus, and H. W. Schcok, Appl. Phys. Letter, **62**, 597, (1993).

[11] S. Shionoya, W. M. Yen, Phosphor Hood book, CRC Press, Boca Raton, FL, (1999), p255.

[12] R. R. Reeber, J. Appl. Phys. **41**, 5063 (1970)

[13] T. Olorunyolemi, A. Birnboim, Y. Carmel, O. C. Wilson, Jr., and I. K. Lloyd, J. Am. Ceram. Soc. **85**, 1249 (2002).

[14] D. C. Look, J. W. Hemsky, J. R. Sizelove, Phys. Rev. letters Vol. **82**, No. 12 (1999).

[15] J. Chennupati and P. Stephen J. "Zinc Oxide Bulk, Thin films and Nanostructures" I^{ts} edition (2006).

[16] C. H. Park, S. B. Zhang, and S. H. Wei, Phys. Rev. B **66**, 073202 (2002).

[17] S. Tu¨zemen, Emre Gu¨ r, Optical Materials **30**, 292–310 (2007).

[18] R. W. Pohl, Einufhrung in die Physik, Vol. **3**, 10th ed., Springer, Heidelberg, (1958).

[19] Y. V. Shaldin and J. Varchulska , Effect of heat treatment on the magnetic properties of hydrothermally Grown ZnO Crystals, Inorganic Materials **39**, 1052 (2003).

[20] V. P. Dotsenko, I. V. Berezozskaya, N. P. Efryushina, et. al., *J. Lumin.* **93** (2001) 13

Chapter 3

Characterization techniques

3.1 X-ray Powder Diffraction

X-ray diffraction (XRD) is a versatile, non-destructive technique used for qualitative and quantitative analysis of a crystalline materials. This experimental technique has been used to determine the overall structure of bulk solids, including lattice constants, identification of unknown materials, orientation of single crystals, orientation of polycrystalline, stress, texture, films thickness etc. In this study, a (Philips X-Ray diffractometer) powder diffraction system with Cu-Kα x-ray tube (λ=1.54056 ^{o}A) was used.

3.1.1 Generation of X-ray

X-rays are short-wavelength, high energy electromagnetic radiation, having the properties of both waves and particles. They can be described in terms of both photon energy (E) or wavelength, λ (lambda – the distance between peaks) and frequency ν (nu – the number of peaks passing a point in a unit of time). The relation between energy, frequency or wavelength in the case of photon is:

$$E = h\nu = \frac{hc}{\lambda} \tag{3.1}$$

Where h and c are Planck's constant and speed of light respectively.

Substituting the values of the constants above in equation yield the following relationship

$$\lambda = \frac{12.4}{E}(KeV) \tag{3.2}$$

X-rays are produced whenever high energy electrons strike with metal target, any x-ray tube must contain;

(a) a source of electron,

(b) a high accelerating voltage,

(c) a metal target,

All x-ray tubes contain two electrodes, an anode (the metal target) usually maintained, at ground potential, and a cathode maintained, at negative potential, normally of order of 30 kV to 50 kV for the diffraction work. Interaction that occur between the beam (i.e. electrons) and target will result in a loss of energy. A continuous spectrum is formed when the high energy electrons are slowed down rapidly by multiple collisions with the anode material, which give rise to white radiation, or so called Bremsstrahlung.

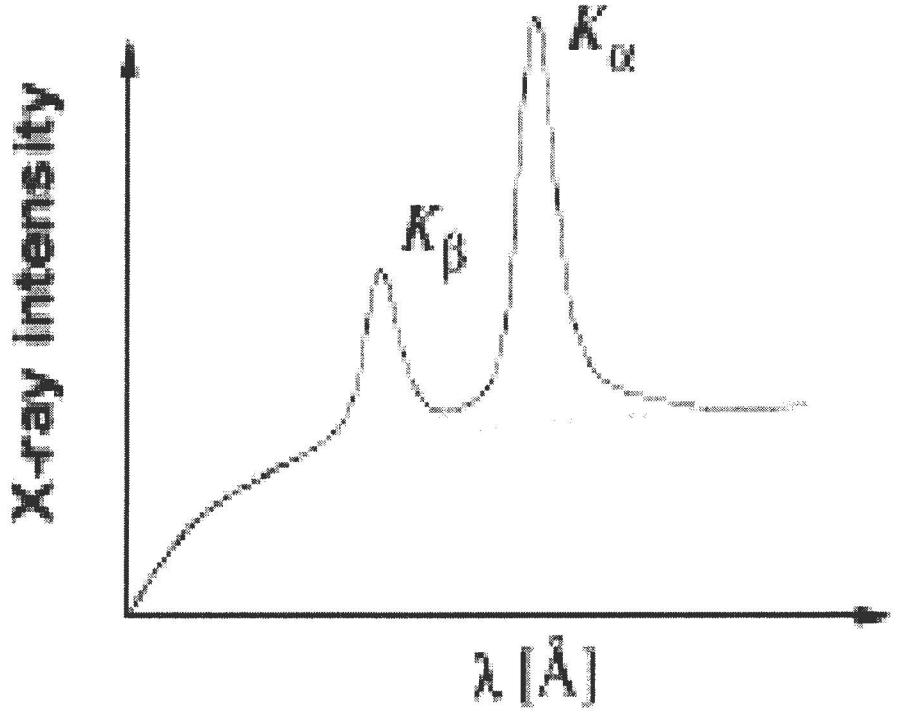

Figure 3.1 X-ray spectrum, with a Bremsstrahlung background and electrons excitations.

The continuous spectrum is formed due to rapid deceleration of the electrons hitting the target, but not every electron decelerates in the same way, some stop in one impact and release all their energy at once, while others deflect this way and that way when they encounter atoms of the target, successively losing fractions of their total kinetic energy until is all spent. Those electrons which are stopped in one impact produce photons of maximum energy (wavelength) equal to the energy loss [1].

3.1.2 Bragg's Law

Since atoms are arranged periodically in a lattice, x-rays scattered from a crystalline solid can constructively interfere, producing a diffracted beam through these atoms. In 1912, W. L. Bragg recognized a predictable relationship among several factors. These factors are combined in Bragg's law:

$$n\lambda = 2d\sin\theta \tag{3.3}$$

n = an interger-1, 2, 3....etc [n=1 for our calculations], λ = the wavelength of the incident X-radiation, in our case, equal to 1.54 Å, d = the distance between similar atomic planes in a mineral (the interatomic spacing) which we call the d-spacing and measure in Å, θ = the diffraction angle in degree.

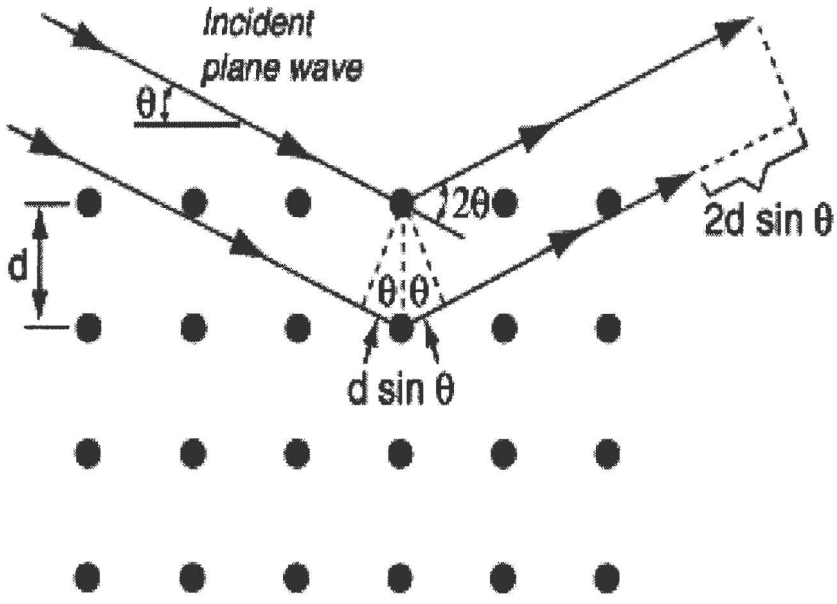

Figure 3.2 Bragg's diffraction condition.

The Ewald sphere construction provides a relation between Bragg's law and the reciprocal space mapping (RSM). RSM is a valuable tool during ω-2θ scan, when strain field exist within the grain. Basically, RSM build on wave vector translation into reciprocal space. The radius of the Ewald sphere is equal to wave vector of the incident X-rays, $|K_{diff}|=2\pi/\lambda$, which is drawn in such a way that it end at the origin of the reciprocal space as shown in figure 3.3. The diffracted beam with wave vector $K_{diff'}$ is determined from $K_{diff} = K_{inc} + G$, where G is the scattering vector, which is normal to the set of plane involved in scattering event. The diffraction condition is fulfilled only if there is a reciprocal lattice point on the Ewald sphere surface at G.

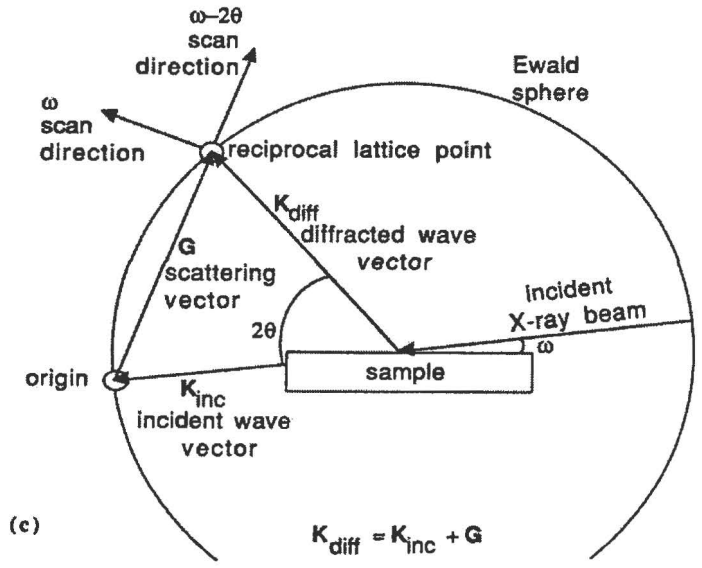

Figure 3.3 Schematic of asymmetric reflection in reciprocal space [24].

3.1.3 Crystallite size measurement

Phase identification using x-ray diffraction depends on the positions of the peaks in a diffraction profile as well as the relative intensities of these peaks to some extent. Another aspect of the diffraction from material is the importance to consider how diffraction peaks are changed by the presence of various types of defects such as small number of dislocations in crystals with dimensions of millimeters. Small size of grain size can be considered as another kind of defect and can change diffraction peak

widths. Very small crystals cause peak broading. The crystallite size is easily calculated as a function of peak width (specified as the full-width at half maximum peak intensity (FWHM)), peak position and wavelength.

Scherer's formula

Suppose that the crystal has a thickness δ measured in a direction perpendicular to a particular set of Bragg planes (Figure 3.4). Let there be (m + 1) planes in this set. Define the Bragg angle as a variable and let θ_β be the angle which exactly satisfies Bragg's law for the particular values of λ and d involved, or

$$\lambda = 2dsin\theta_\beta \tag{3.3}$$

In the Figure 3.4, rays **A**, **D**... **M** make exactly this angle θ_β with the diffraction planes. Incident x-rays that make angles only slightly different from θ_β produce incomplete destructive interference. Ray **B**, for example, makes a slightly larger angle θ_1, such that ray **L'** from the mth plane below the surface is (m + 1) wavelengths out of phase with **B'**, the ray from the surface plane. The intensity of the beam diffracted at an angle $2\theta_1$ is therefore zero. It is also zero at an angle $2\theta_2$ where θ_2 is such that ray **N'** from the mth plane below the surface is (m - 1) wavelengths out of phase with ray **C'** from the surface plane. This defines, therefore, the two limiting angles, $2\theta_1$ and $2\theta_2$, at which the diffracted intensity must drop zero.

The curve of diffracted intensity vs. 2θ will thus have the form of Figure 3.5a in contrast to Figure 3.5b, which illustrates the hypothetical case of diffraction occurring only at the exact Bragg angle. The width of the diffraction curve of Figure 3.5a increases as a thickness of the crystal decreases, because the angular range ($2\theta_1$ - $2\theta_2$) increases as m decreases. The width β is usually measured, in radians, at intensity equal to half the maximum intensity (FWHM).

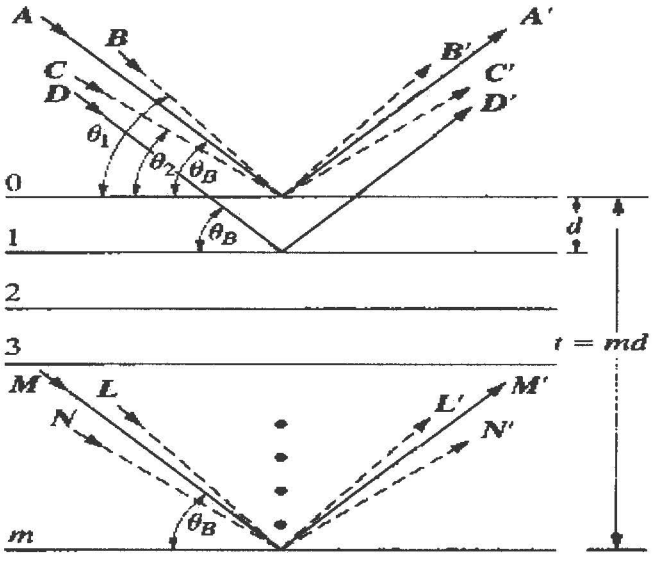

Figure 3.4 Effect of crystal size on diffraction [1].

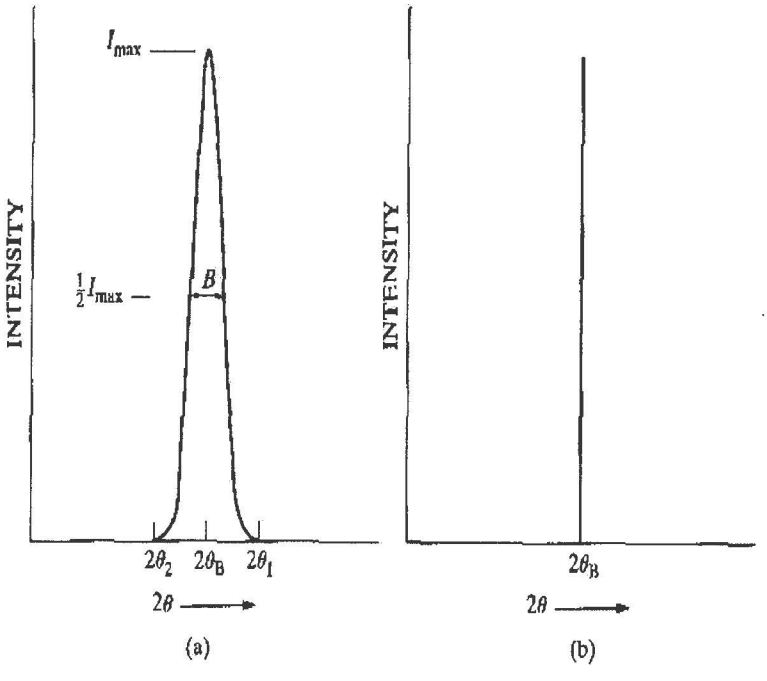

Figure 3.5 Effect of fine crystallite size on diffraction curves [1]

Therefore;

$$\beta = \frac{1}{2}(2\theta_1 - 2\theta_2) = \theta_1 - \theta_2$$

The path-difference equations for these two angles are similar, but related to the entire thickness of the crystal rather than to the distance between adjacent planes:

$$2dsin\theta_1 = (m+1)\lambda$$

$$2dsin\theta_2 = (m-1)\lambda$$

By subtraction,

$$2dcos\ \frac{(\theta_1+\theta_2)}{2} sin\frac{(\theta_1-\theta_2)}{2} = \lambda$$

But θ_1 and θ_2 are both very nearly equal to θ_β, so that $\theta 1+\theta 2 = 2\theta_\beta$

and $$Sin\frac{(\theta_1-\theta_2)}{2} = \frac{(\theta_1-\theta_2)}{2}$$ (approx.)

Therefore; $$2\delta\frac{(\theta_1-\theta_2)}{2}Cos\theta_\beta = \lambda$$ or, $$\delta = \frac{\lambda}{\beta_{1/2}}Cos\ \theta_\beta$$

A more exact treatment of the problem gives:

$$\delta = \frac{0.9\lambda}{\beta 1/2}Cos\theta_\beta \qquad (3.4)$$

This is known as Scherrer's formula. It is used to estimate the size of very small crystals from measured width of their diffraction curves. Note that whether a value of 0.9 or 1 is used depends on shapes of the crystallites assumed to be sample.

3.1.4 Determination of lattice parameters

For the wurtzite structure the interplanar distance of {hkl} plane is related to the lattice parameters *a* and *c* via the Miller indices *hkl*:

$$\frac{1}{d_{hkl}} = \frac{4}{3}\left(\frac{h_2 + k_2 + hk}{a_2}\right) + \frac{l_2}{c_2} \tag{3.5}$$

For the lattice parameters determination for a c-plane oriented sample includes a measurement of d_{001} in order to determine the *c* lattice parameter, and for the determination of a lattice from a second measurement of d_{hkl} with either *h* or *k* different from zero [3]

3.2 Scanning electron microscopy (SEM) and energy dispersive x-ray spectroscopy (EDS)

Scanning electron microscopy (SEM) is basically a type of electron microscope. SEM is used for various purposes;

- Morphology studies,
- Microstructure analysis,
- Elemental analysis if equipped with appropriate detector (energy/wavelength dispersive x-rays),
- Chemical composition,
- Elemental mapping,

The morphology of the prepared ZnO powders was examined by SEM using a Shimadzu SSX-550 SEM: Superscan model. Samples for the SEM examination were prepared by mounting a double sticking carbon tape on the stub. The particles were then dispersed on top of the tape. The stubs were then loaded into the instrument and ready for characterization.

3.2.1 SEM set-up

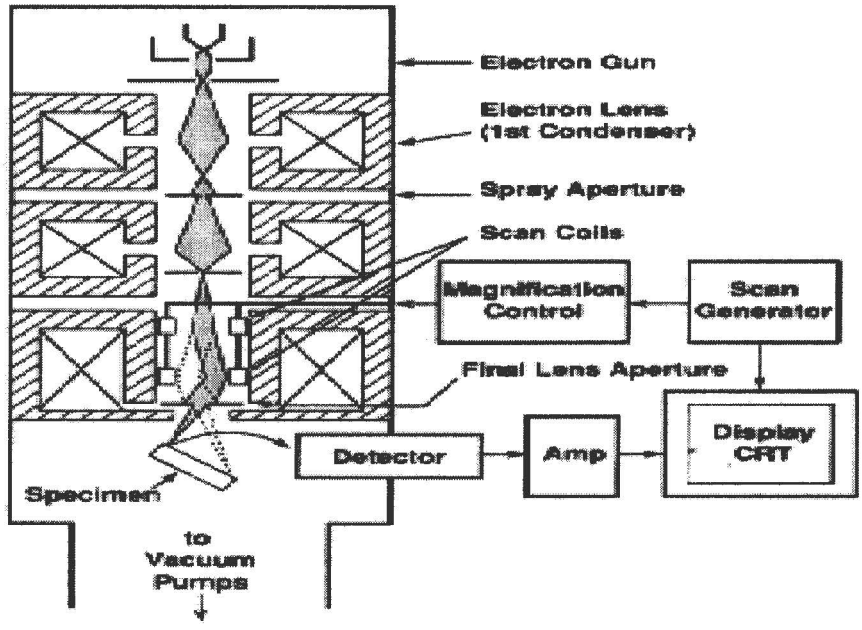

Figure 3.6 *Schematic drawing showing the electron column, the deflection system and the electron detectors*

The SEM process starts with the electrons emitted from the electron gun. The electron beam, which typically has an energy ranging from a few hundred eV to 100 keV, is attracted to the anode, condensed and focused by the condenser lens and the objective lens into a beam with a very fine focal spot. The beam passes through pairs of scanning coils or pairs of deflector plates in the electron optical column, typically in the objective lens, which deflect the beam horizontally and vertically so that it scans in a raster fashion over a rectangular area of the sample surface. After hitting the sample, the beam produces, among others, secondary and backscattered electrons from the sample. These electrons are collected by a secondary electron or a backscattered electron detector, converted to a voltage, and amplified. A detector is used to convert X-ray energy into voltage signals; this information is sent to a pulse processor, which measures the signals and passes them onto an analyzer for data display and analysis. The beam scanning the sample surface and the display beam are synchronized. The elemental composition was determined using the same SEM instrument equipped with

energy dispersive x-ray spectroscopy (EDS) capability. The EDS operates with a LINK AN10000 detection system with an ultra-thin window for light element analysis. EDS analysis utilizes characteristic x-rays coming from the surface when the high energy electrons strike the sample. Normal operating acceleration voltages, to generate the high energy electrons, range between 20 and 30kV. The penetration depth of the electrons into the sample depends on the acceleration voltage. The generated x-ray photons enter a lithium drifted silicon detector, Si (Li), in which electron-hole pairs are created. An electron from an outer, higher-energy shell then fills the hole, and the difference in energy between the higher energy shell and the lower energy shell is released in the form of an X-ray. The x-ray released by the electron as shown in Figure 3.7 is then detected and analyzed by the energy dispersive spectrometer. These x-rays are characteristic of the difference in energy between the two shells, and of the atomic structure of the element from which they were emitted.

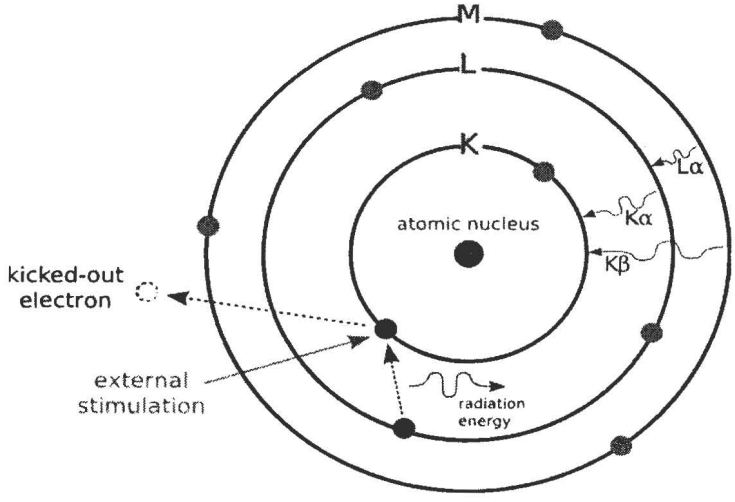

Figure 3.7 *A figure showing the ejection of an electron from the inner shell*

3.3 Photoluminescence

Photoluminescence (PL) is a powerful and a relatively simple method, extensively used as characterization technique of semiconductor physics for a number of reasons [23, 24].

- It is non-destructive because it is based on pure optical processes,
- No sample preparation is required,
- Highly sensitive,
- Detailed information on the electronic structure in the semiconductor can be deduced from the experiments.

Information that could be deduced from a PL study includes the size of the band gap, impurity levels, interface, and surface properties as well as density of states and excitonic states. Basically in PL measurements, a semiconductor sample is optically excited by an excitation source such as a laser which produces photons having energies larger than the band gap of the semiconductor. The incident photons are absorbed under creation of electron-hole pairs in the sample. After a short time the electrons eventually recombine with the holes, to emit photons, and light or luminescence will emerge from the sample. The energy of the emitted photons reflects the energy carrier in the sample. The emitted luminescence is collected, and intensity is recorded as a function of the emitted photon energy, to produce a PL spectrum. In a PL measurement, the excitation energy is kept fixed, while the detection energy is scanned. The energy of emitted photon is characteristic for radiative recombination process.

PL technique is particularly helpful in the analysis of discrete defect and impurity states. To gain more knowledge about the electronic structure, magnetic and electric fields can be applied in a controlled manner. Moreover external forces can be used in PL investigations, e.g. the strain by exposing the material to mechanical pressure. Since PL relies on radiative recombination, so it is very difficult for the investigation of non-radiative processes needs indirect methods, and the material having poor quality are hard to characterize through PL.

3.3.1 Radiative recombination mechanisms observed in PL

In semiconductors, the luminescence can be achieved by several radiative transitions between the conduction band and valence band, exciton, donor and acceptor levels, as shown in figure 3.8. Upon excitation at energy above the bang gap, free electrons are created in the conduction band together with the free holes in the valance bond. These carriers will energetically relax down the band edge. Due to mutual coulomb interaction,

electron-hole pair is formed. This electron-hole is usually called a free exciton (FE). Its energy is slightly smaller than the bang gap energy. This energy difference is the binding energy of the free exciton. A neutral donor (acceptor) will give rise to an attractive potential, a free exciton might be captured at the acceptor (donor). A bound exciton (BE) is formed.

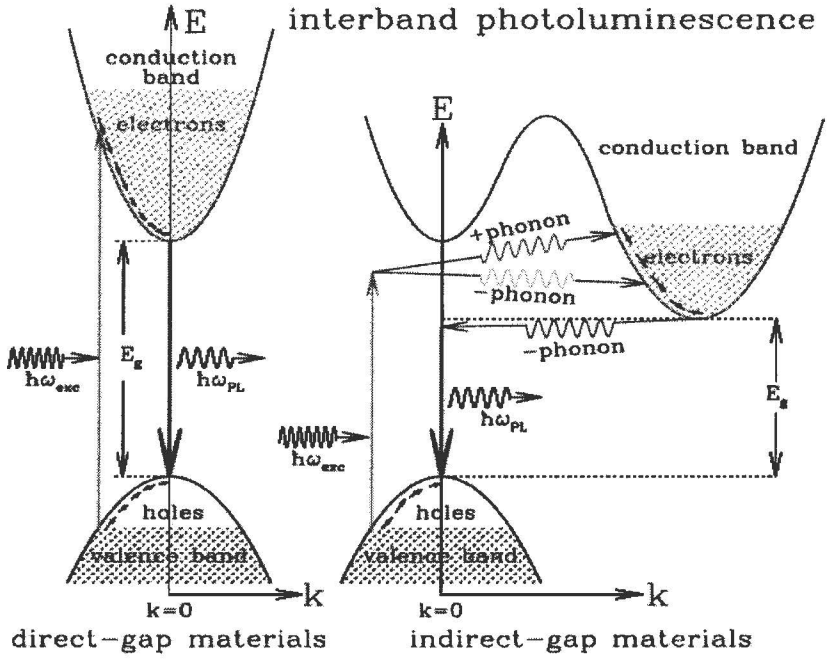

Figure 3.8(a) Schematic illustration of common recombination processes [22].

An electron bound to a donor can recombine directly with a free hole from a valence band. This kind of recombination is called free-to-bound (FB) transition. The recombination energy for such a transition corresponds to the band gap energy reduced with the binding energy of donor. Another possibility is that a hole bound to an acceptor recombines with an electron bound to a donor in donor-acceptor pair (DAP) transition. Both the donor and the acceptor are neutral before the recombination (i.e. the donor positively and the acceptor negatively charged).

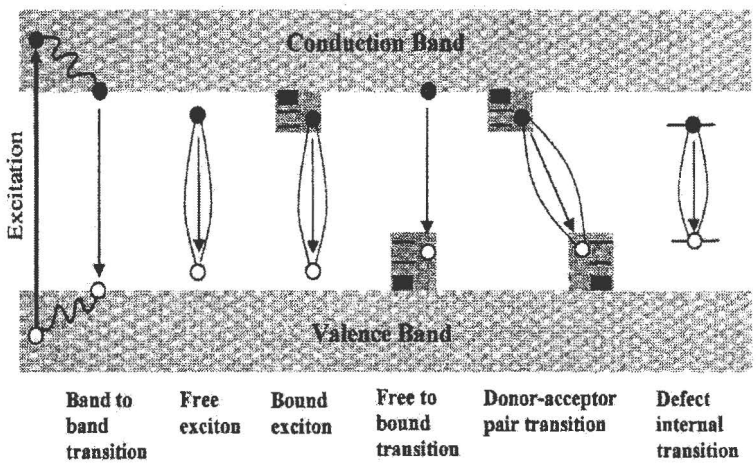

Figure 3.8(b) Schematic illustration of common recombination processes [22].

Thus there is a Coulomb interaction between the donor and acceptor after the transition and extra Coulomb energy is gained in the final state added to the radiative recombination energy. The transition energy E (R) depends on the distance R between the donor and acceptor atoms.

3.3.2 Micro-photoluminescence spectroscopy

High spatial resolution is gained in the micro-PL by replacing the lens focusing the laser on the sample by a microscope objective. The microscope objective offers the possibility to focus the laser spot down to 2μm in diameter and gives the value up to μm-precision in the sample position. The focusing of the light is managed by moving the objective, while the cryostat, which makes possible measurement at very low temperature, is adjusted vertically and horizontally to change the position of the excitation spot. A magnified image of the sample is taken from the CCD-chip of a video camera, allowing precise control of laser focusing and sample position.

3.3.3 Experimental setup

The experimental setup consists of an excitation source, cryostat, microscope objective, monochromator, CCd-TV camera and additional components [21].

Excitation source

Excitation source is usually a laser, which provides a stable and well defined source of the monochromatic light. The fourth harmonic of CW Nd: Vanadate laser (266) can be used.

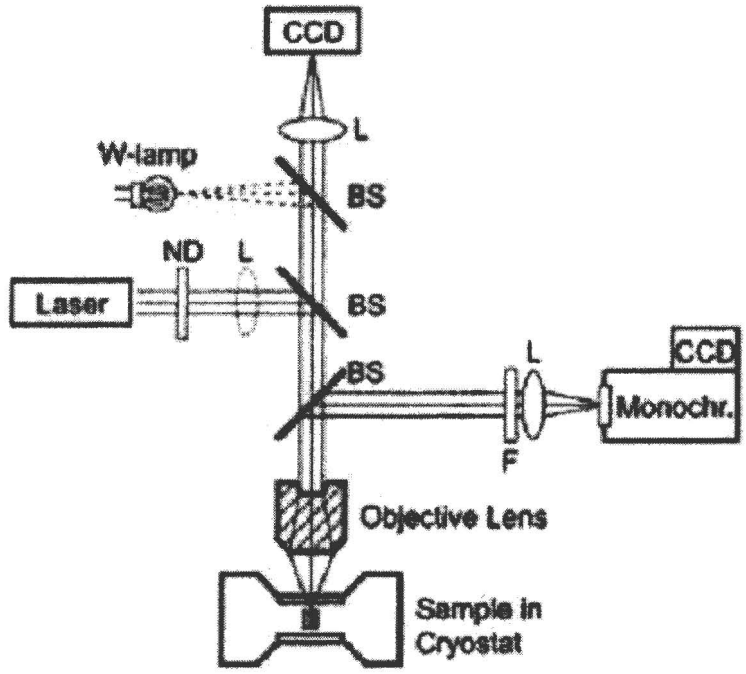

Figure 3.9: Schematic illustration of the μ-PL.

Cryostat

The cryostat is used to cool the sample to a low temperature. The sample is mounted inside the continuous He-flow close to the glass window. This allows adjusting microscope objective at the focal point of the microscope to get the smallest laser spot

size (1μm). We used the vacuum pump to decrease the pressure above the helium surface. The temperature can be varied from 2-300K.

Microscope objectives

The microscope objective, outside the cryostat is used for both by focusing laser light excite and collect the emitted light from the sample. By using beam splitters and mirrors the collected light is guided to spectrometer and detector.

Monochromator

The monochromator was used to choose wavelength that will reach the detector at the exit of slit of the monochromator. Single monochromator of 0.55 m with 2400 gratings with a spectral resolution < 0.2 meV at 360nm can be used.

Video camera

Video camera is used for obtaining an image of the surface on the monitor. This is achieved by illuminating the sample with white light lamp through the microscope objective and detecting light from the sample. The camera helps us to locate the sample and guarantees that we are measuring at the same sample position. The camera also shows the laser spot and helping in obtaining the optimal alignment of the setup.

References

[1] B. D. Cullity and S. R. Stock, "Element of x-ray diffraction" 3rd edition, Practice-Hall Inc. New Jersy. (2001)

[2] M. R. Sardela Jr., "The growth, thermal stability, structural and electrical properties of doped and undoped Si-based epitaxial structures" PhD thesis Linköping University Press, Dissertation No.341 (2000).

[3] D. Vanya, "Strain-related structural and vibrational properties of group-III nitride layers and super lattices" PhD thesis linköping university Dissertation No.891 (2004)

[4] O. Milton, "Materials science of thin films, deposition and structure" 2nd edition.

[5] P. R. Berman, "Advanced in atomic, molecular and optical physics", Vol.**45** (Academic press, Amsterdam, 1997)

[6] L. Mats, "Spectroscopy of semiconductor quantum dots" PhD thesis Linkoping universities Dissertation No.976 (2005)

[7] L. T. Lin, Y. Hu and T. H. Hsieh, *Rev.Adv.Mater.Sci*, **5** (2003) 464

[8] T. Fukuyo and H. Imai, *Journal of Crystal Growth,* **241** (2002) 193

[9] K. D. Kim, D. N. Han and H. T. Kim, *Chemical Engineering Journal,* **104** (2004) 55

[10] M. Rong, M. Zhang, H. Lui and H. Zeng *Polymer,* **40** (1999) 6169

[11] G. Carotenuto, G. P. Pepe and L. Nicolais, *Eur. Phys.J.,* **16** (2000) 11

[12] C. Luo, Y. Zhang, X. Zeng, Y. Zeng and Y. J .Wang, *Colloid Interface Sci.*, **288** (2005) 444

[13] Y. Lu, Mei, M. Dechsler and M. Ballanff, *Angew. Chem. Int. Ed.,* **45** (2006) 813

[14] M. Muniz-Miranda and M. Innocenti, *Applied Surface Science,* **226** (2004) 125

[15] K. S. Chou and Y. S. Lai, *Materials Chemistry and Physics,* **83** (2004) 82

[16] H. Chen, Y .Wang, S. Dong and E. Wang, *Spectrochimica Acta Part A,* **64** (2006) 343

[17] Z. Gryczynski, J. Lukomska, J. R. Lakowicz, E.G. Matveeva, I Gryczynski, *Chemical Physics Letters,* **421** (2006) 189

[18] W. Songping and M. Shuyuan, *Materials Chemistry and Physics,* **89** (2005) 423

[19] L. Suber, I. Sondi, E. Matijević and D. V. Goia, *Journal of Colloidal and Interface Science,* **288** (2005) 489

[20] A. Sileikaite, I. Prosycevas, J. Puiso, A. Juraitis and A. Guobiene, *Materials Science (Medziagotyra),* **12** (2006) 287

[21] P. Justinas, "Photoluminescence excitation spectroscopy of single self-assembled InAs/GaAS quantum dot" Master thesis Lith-IFM-07/1839-SE.

[22] Q. Nguyen, "Thin optically detected magnetic resonance studies of intrinsic defects in dilute" PhD thesis linköping university Dissertation No.901 (2004)

[23] P. R. Berman, "Advanced in atomic, molecular and optical physics", Vol.**45** (Academic press, Amsterdam, 1997)

[24] M. R. Sardela Jr., "The growth, thermal stability, structural and electrical properties of doped and undoped Si-based epitaxial structures" PhD thesis Linköping University Press, Dissertation No.341 (2000).

Chapter 4

Synthesis and characterization of ZnO nanoparticles by varying the sodium hydroxide to zinc acetate molar ratios by a Sol-Gel process

4.1 Introduction

Semiconductor nanoparticles are a very important topic in the ongoing research activity across the world [1]. The semiconductor particles exhibit size-dependant properties such as scaling of the energy gap and corresponding change in the optical properties. They are considered as the front runners in the technologically important materials. ZnO is attracting tremendous attention due to its electronic properties. It has a wide and direct band gap of 3.37 eV at room temperature and it has a large exciton binding energy of 60 meV. As a result of its excellent chemical and physical properties [1–5], ZnO has been widely used in low-voltage phosphor material, sensors, photovoltaic, photonics, light-emitting devices, photo detectors, optical waveguides, transparent conductive films, and bulk acoustic wave devices [6–9]. ZnO as luminescent nanomaterials in the form of nanoparticles, nanorods, nanowires, nanotubes, nanocomposites as well as colloidal or bulk nanocrystals are of interest not only for basic research but also for usable applications [10-12]. High surface to volume ratio, local phenomena such as absorption or change in the surface electronic state may contribute significantly to special properties.

Many methods have been developed to prepare ZnO particles, including the sol–gel method [10], evaporative decomposition of solution [11], template-assisted growth [12], wet chemical synthesis [13], and gas-phase reaction [14]. Generally, some of the above methods require complex equipment and complicated operation, which can be called 'noble' methods. It is still a challenge to search for a simple, cheap, scalable and reproducible route to prepare metal oxides nanoparticles with a high yield and superior qualities. Herein, we report a simple sol-gel method in ethanolic solution to prepare ZnO

nanoparticles. The influences of the molar ratio of OH^-/Zn^{2+} on structural, morphological and optical properties of the dried pure ZnO nanoparticles were investigated.

4.2 Experimental

ZnO nanoparticles were prepared in an ethanol medium by the reaction of zinc acetate ($Zn(CH_3COO)_2$) and sodium hydroxide (NaOH). All chemicals used were AR grade and not further treated. The detailed preparation procedure may be summarized as follows: 0.918g of $Zn(CH_3COO)_2$ was dissolved in 60 ml of ethanol using vigorous magnetic stirring at 80 °C for 30 min followed by cooling in ice water for 5 min. To determine the dependence of the prepared ZnO nanoparticles on the NaOH content of the precursors various weights of NaOH pellets (as shown in Table 4.1) were dissolved in 20 ml of ethanol in a preheated ultrasonic bath to change the PH of the solution, and cooled in ice water as well. These solutions were slowly added to the Zn^{2+} solution using vigorous stirring in ice water. After centrifugally separated from the solutions, repeatedly washed using a mixture of ethanol and heptanes, and then dried, white powders of the nanoparticles were obtained. The precipitates were dried at ambient condition in a fume cabinet for 2 days. The X-ray diffraction (XRD) patterns were recorded to characterize the phase and crystal structure of the nanoparticles using a multi-purpose XRD system with a Siemens Diffractometer D5000 with a Cu K_α radiation source at 40 kV, 30 mA and λ = 1.5418 Å. The morphology of the nanoparticles was observed by a Shimadzu Superscan SSX-550 system scanning electron microscope (SEM) operated at 20 kV equipped with energy dispersive X-ray spectroscopy (EDS). To determine the annealing and crystallization temperature of the as prepared ZnO nanoparticles, the thermal analysis was carried out with a Perkin-Elmer DSC 7 differential scanning calorimeter (DSC), and Thermo gravimetric analyses (TGA) were performed in a Perkin-Elmer TGA7 thermo gravimetric analyzer. Transmission electron microscope (TEM) images were recorded on a Philips EM420 transmission electron microscope. Optical absorption was performed on an Agilent HP1100 diode-array UV-visible spectrophotometer. Room temperature photoluminescence (PL) of the samples was measured, using a He–Cd laser (325 nm) as excitation sources.

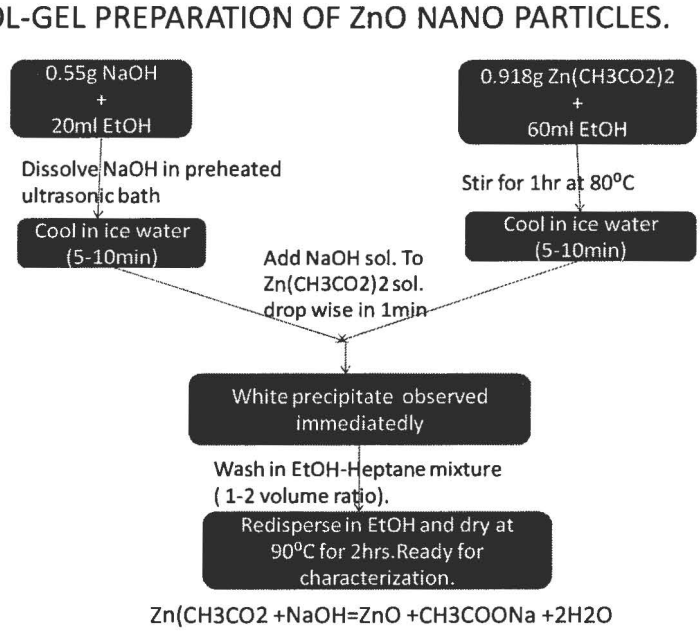

Figure 4.1 SOL-GEL PREPARATION OF ZnO NANOPARTICLES.

Table 4.1 Composition of precursors for different ZnO nanostructures

Precursors	No. of moles of NaOH	No of Moles of $Zn(CH_3COO)^2$ x 10^{-3}	OH^-/Zn^{2+} Molar ratio	PH
1	0	3.15	0	5.6
2	5.5×10^{-3}	3.15	1.7	8.1
3	8.25×10^{-3}	3.15	2.6	10.1
4	1.1×10^{-2}	3.15	3.5	11.4
5	1.375×10^{-2}	3.15	4.4	11.5
6	1.65×10^{-2}	3.15	5.2	11.4
7	1.925×10^{-2}	3.15	6.1	11.5
9	2.2×10^{-2}	3.15	7	11.4

4.3 Results and discussions

4.3.1 Thermal properties

TGA – DSC curves of as deposited ZnO nanoparticles are shown in Fig. 4.2. There was a total weight loss of 13 wt. % when the sample was heated from room temperature to 350 °C. Three weight losses were observed in the temperature regions RT – 60 °C, 90 – 120 °C and 150 – 350 °C. Weight loss of about 2 wt. % from room temperature to 60 °C was due to desorption of the physically adsorbed water and partly chemically adsorbed alcohol. The weight loss of 7 wt. % from 90 to 120 °C was due to the removal of chemically adsorbed water and alcohol. Weight loss of almost 3 wt. % from 120 to 350 °C was mostly due to the decomposition of organic matter and the hydroxide groups. Two endothermic peaks (100 °C; 192 °C) were found in the heating process. The endothermic peak at 100 °C in DSC results from evaporation of solvent. The broad endothermic peak around 192 °C results from the decomposition of residual organics and crystallization of ZnO. There is a slight gradual weight loss of ZnO after 250 °C as observed from TGA curve. Hence the as prepared ZnO samples are annealed at 600 °C for crystallization.

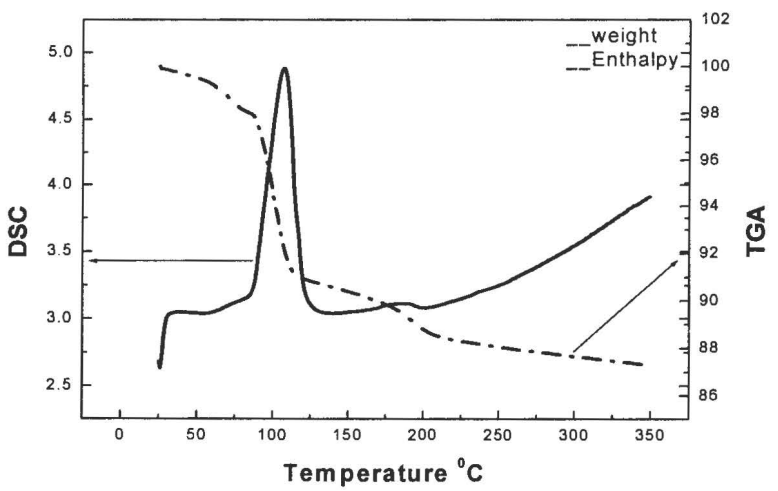

Figure 4.2 DSC-TGA heating curves of the ZnO nanoparticles samples from 23 to 350 ^{0}C.

4.3.2 Morphological and structural properties

The morphology and size of the dried ZnO nanoparticles were examined by SEM observations. By adjusting the OH^-/Zn^{2+} molar ratios, many ZnO nanostructures with approximately similar morphological properties were obtained, in particular the range of the molar ratios were investigated.

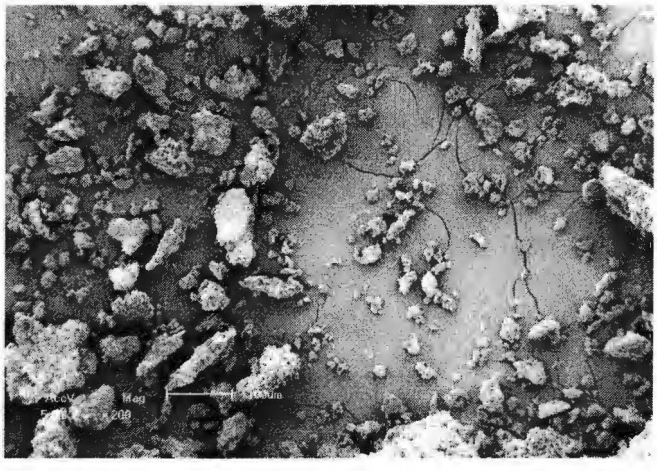

Figure 4.3 SEM image of agglomerated ZnO.

A representative SEM image of ZnO powder dried at ambient conditions in a fume cabinet for 2 days is presented in Fig. 4.3. The presence of some bigger particles should be attributed to the aggregating or overlapping of smaller particles. However, small agglomerates on some of the large particles are clearly visible at high magnifications. Therefore it is concluded that the chosen OH^-/Zn^{2+} molar ratio range has minimum influence on the morphology of the ZnO samples. Fig. 4.4 shows the TEM image of ZnO nanopowders with OH^-/Zn^{2+} molar ratio equal to 1.7. As shown in the figure the powder was monodispersed with nearly spherical nanoparticles with a mean size of between 5 and 20 nm. The presence of some bigger particles should be attributed to the aggregating or overlapping of smaller particles. The TEM observations further confirmed the calculated average size of ZnO nanoparticles with OH^-/Zn^{2+} molar ratio equal to 1.7.

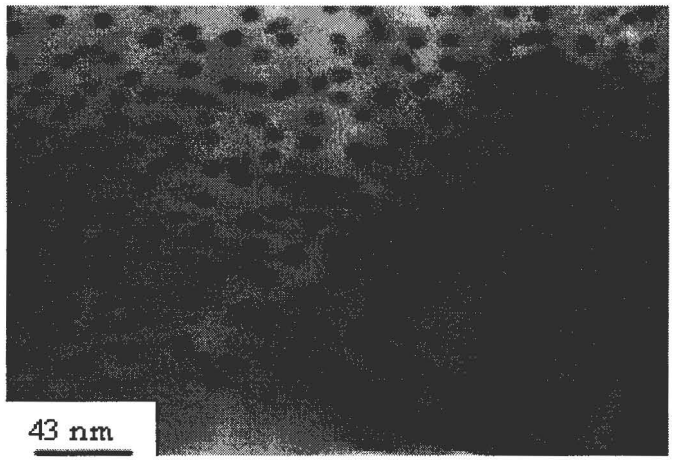

Figure 4.4 TEM image of dried ZnO nanoparticles.

To determine the elemental composition of our matrices, EDS spectra were taken. For all ZnO samples which were dried for 2 days in air, all expected elements (Zn, O) were detected and the adventitious carbon is also to be seen as shown in Fig. 4.5. Fig.4. 6 shows the XRD pattern obtained from a typically dried ZnO powder. The results indicate that ZnO has been successfully prepared by a sol-gel process. The observed diffraction peaks are well-matched with the typical single crystalline wurtzite hexagonal phase bulk ZnO (JCPDS, card no. 36-1451). No other peaks of impurities such as Zn or Zn $(OH)_2$ were detected within the detection limit of the X-ray diffraction instrument. The intense and sharp peaks in the diffraction spectrum show the high-crystallinity of the dried powders. The peaks are broad due to the nanocrystalline nature of the obtained powder. The average grain size (D) of the prepared nanoparticles was calculated using Debye–Scherrer formula [15]:

$$D = \frac{0.9\lambda}{\beta \cos\theta}$$

where $\lambda = 0.154$ nm is the wavelength of the X-ray radiation used, θ the Bragg diffraction angle of the XRD peak and β is the measured broadening of the diffraction line peak at an angle of 2θ, at half its maximum intensity (FWHM) in radians. It is found that the average grain size reduced with molar ratio until $OH^-/Zn^{2+} = 4.4$ and increased again as the molar ratio increased.

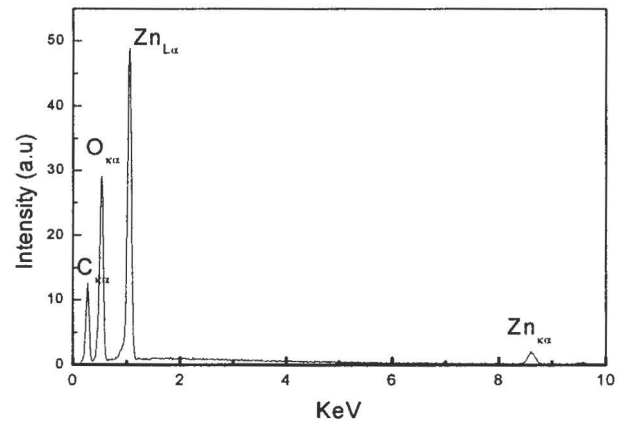

Figure 4.5 EDS spectra of dried ZnO nanoparticles.

The average grain size was estimated as 10.3 nm for OH^-/Zn^{2+} molar ratio equal to 1.7, 8.8 nm for 4.4, 11.5 nm for 5.2 and 44 nm for 7. The results are partly in agreements with the absorption spectra examined by Sakohara *et al.* [16], who claimed that the particle size increased with the lithium hydroxide concentration for the range investigated. It is concluded that the particle size of the ZnO nanoparticles are dependent on the amount of NaOH added.

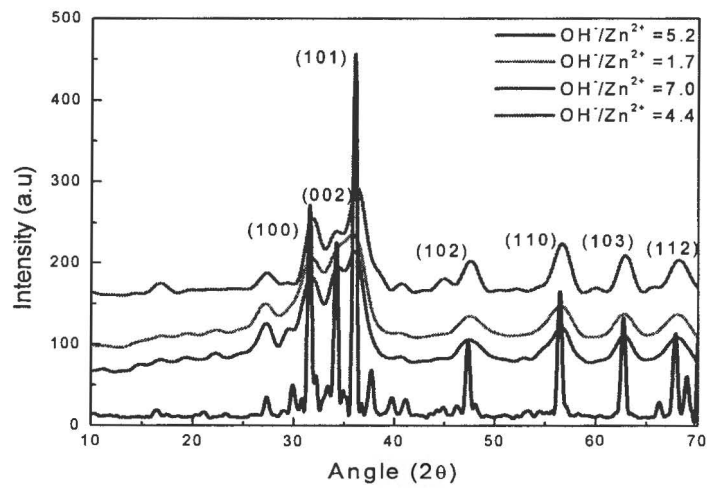

Figure 4.6 X-ray diffraction spectrum of the prepared ZnO nanoparticles using different molar ratio of OH^-/Zn^{2+}.

The calculated nanoparticle sizes for ZnO sample with OH^-/Zn^{2+} molar ratio of 1.7 corresponds well to that depicted by the TEM image of the said sample. Similar results have been reported by Abdullah *et al.* [17] and Ntwaeaborwa and Holloway [18] from ZnO colloid prepared by hydrolysis method and sol gel synthesized ZnO nanoparticles respectively.

4.3.3 Optical properties

Figure 4.6 shows UV-Vis optical absorption spectra of the dried ZnO samples. In general absorption and transmission spectra probe the crystalline internal molecular orbital and provide information concerning size and particle compositions [18]. The absorbance decreases (band gap increases) with an increase in OH^-/Zn^{2+} molar ratio up to 8.8, but for OH^-/Zn^{2+} molar ratio of 4.4 its distinctively high. It is clearly visible from absorbance spectra that the excitonic absorption peak of ZnO nanoparticles appears around 360 nm for selected molar ratios, which lies much below the bandgap wavelength of 375 nm (E_g = 3.3) of bulk ZnO [16], indicating that the particles must be comparable to the Bohr radius of exciton for ZnO. It is also observed that absorption edge of ZnO is very sharp for OH^-/Zn^{2+} molar ration of 0.44, 0.55 and 0.88 that indicates the monodispersed nature of the nanoparticle distribution [19]. The monodispresed nature of particle distribution for OH^-/Zn^{2+} molar ration of 1.7 have also been confirmed by TEM measurement as shown in Fig. 4.4. The relatively high absorbance at longer wavelengths and broad absorption edge for OH^-/Zn^{2+} molar ration of 0.22 indicates large dispersion in size of the ZnO nanostructures and their arbitrary orientations. Combination of low visible absorbance displayed by the ZnO nanoparticles and low electrical resistivity is very useful in applications such as transparent electrodes in solar cells, luminescence display screens and ultraviolet diodes [16]. Insert in Fig.4. 6 depicts plot of α^2 versus *hv* for as deposited ZnO nanoparticles. The extrapolation of the linear portion of $(\alpha hv)^2$ versus *hv* graph at α = 0 yields the band gap value of the nanoparticles [20, 21]. The band gap of prepared ZnO around 3.3 eV agrees well with the values generally reported in literature [16]. It can also be seen from Fig. 4.6 that band gap value slightly increases to approximately 4.1 eV with an increase in OH^-/Zn^{2+} molar ratio but for molar ratio of 4.4 its relative high.

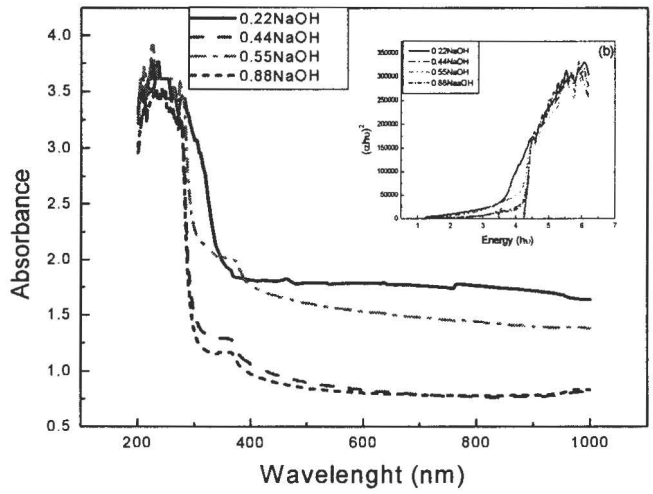

Figure 4.6 UV-VIS absorption characteristics of ZnO nanopartilces dispersed in distilled water. Inset shows the $(\alpha h\upsilon)^2$ vs. $h\upsilon$ graph.

Fig. 4.7(a) shows the PL emission spectra for the ZnO powder excited with a He–Cd laser (325 nm). Clearly, two bands were observed from the room-temperature PL spectrum of the ZnO nanoparticles for molar ratio of 1.7 i.e., blue emission and green – yellow emission at 468 and around 580 nm, respectively. Interestingly, it was observed that, in all other cases, the green emission is enhanced while blue luminescence is quenched and completely disappear in most cases with variation in molar ration. The results confirm broad luminescence in the green – yellow region [18] for ZnO powder. Regarding the appearance of blue emission in ZnO nanomaterials, Dai *et al* reported that blue emission at 460 nm might be due to intrinsic defects such as oxygen and zinc interstitials [22]. However, the exact mechanism behind this emission is still unclear. The green emission is also known to be a deep level emission which is caused by the impurities and structural defects in the crystal such as oxygen vacancies, zinc interstitials, etc. Vanheusden *et al* proposed the mechanism of green emission and reported that green emission is due to the recombination of the electrons in singly occupied oxygen vacancies in ZnO and that the emission results due to the

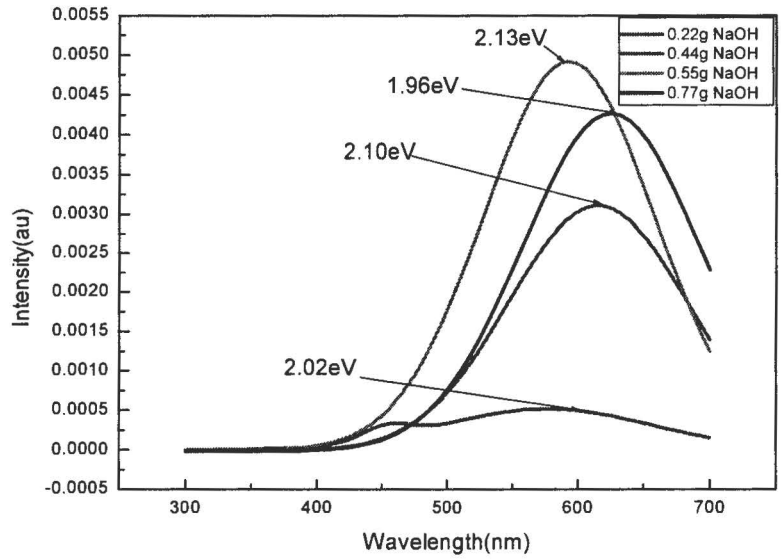

Figure 4.7(a) PL emission spectra of ZnO nanoparticles prepared by various concentration of NaOH in the precursor.

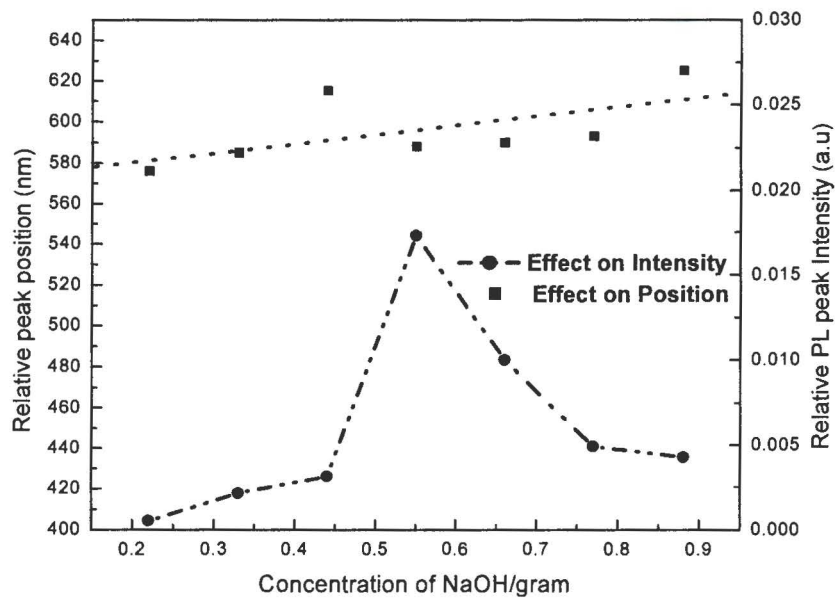

Figure 4. 7(b) Effect of NaOH concentration on the intensity of the broad PL peaks and corresponding emission wavelength.

recombination of a photo-generated hole with an electron occupying the oxygen vacancies.

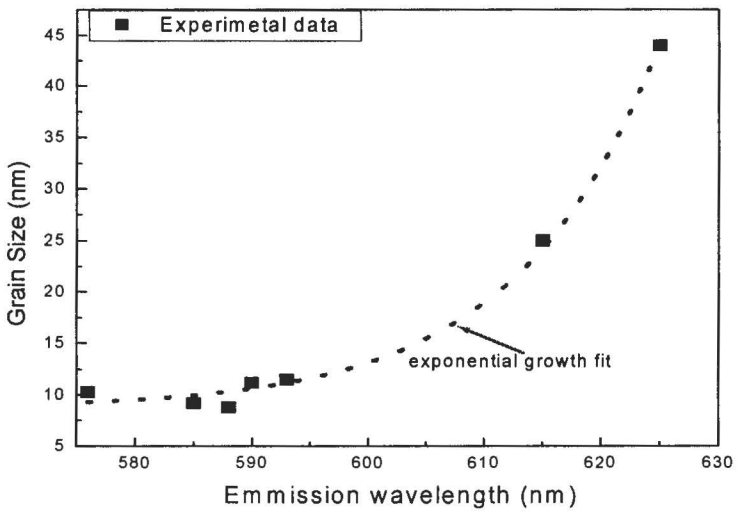

Figure 4.7(c) The dependence of emission wavelength (energy) on the NaOH concentration.

As shown in Fig. 4.7(b), the intensity of the broad green PL peak and the corresponding emission peak position were also affected by the OH^-/Zn^{2+} molar ratios in the precursor solution. As the molar ratio increases to about 5.5, the green luminescence intensity increase to maximum value and then reduces thereafter. On the contrary the relative peak positions of green emission portray on average a linear relationship with concentration of NaOH. Fig. 4.7(c) shows that the emission wavelength (energy) has an exponential increase with the grain size. The increases in emission energy are attributed to the particle size variation of the dried ZnO nanoparticles as the molar ratios of OH-/Zn2+vary. The decrease in particles size increase the band gap energy, correspond to a larger transition energy from the valence band to the location of delocalized electrons at singly occupied oxygen vacancies within deep trapped holes. It was observed therefore that not only does the molar ratio of OH^-/Zn^{2+} of the precursor influence the size of the prepared nanoparticles, but also significantly control the emission energy and maximum luminescence intensity. It is argued that particles

surface depletion plays a major role in the density of singly ionized oxygen vacancies and the charge state of this defect and thus is controlling the green emission intensity [23, 24]. This suggests they originate from different sites in the ZnO phosphor. The visible luminescence in ZnO has been proposed to be caused by the breakage of excitons whereby an electron decays non-radiatively to the defect states in the optical gap and then radiatively recombining with the holes at the valency band. In nano-crystalline ZnO, due to increase in the surface area/volume ratio, the luminescence from the defect states is large. For device application therefore such defect states should be controlled to reduce the visible deep level emission.

4.4 Conclusion

In summary, high quality luminescent ZnO powder with different sizes was prepared by wet chemical synthesis through a sol gel process just by adjusting the molar ratio of sodium hydroxide to zinc acetate. XRD confirmed the wurtzite structure of ZnO. All elements expected in the nanoparticles were observed through EDX. SEM showed agglomerated particles albeit with nanosized agglomerates on the surface and which were interpreted as the building particles of the bigger ones. A further indication to nanosized particles of the ZnO powder was revealed by the TEM image, increase in band gap and blue shifted luminescence of both UV-vis and PL measurements. The deep level defect emission luminescence is predominant for the prepared ZnO nanoparticles by sol-gel, while the intensity of the green emission luminescence is optimum for OH^-/Zn^+ molar ratio of 4.4. This enhanced luminescence was attributed to quantum confinement caused by the nano sized ZnO nanoparticles. The choice of appropriate molar ratio of the precursor is paramount in the size control of ZnO nanoparticles as no catalyst is employed.

References

[1] J. Joo, S. G. Kwon, J. H. Yu and T. Hyeon, 2005 *Adv. Mater.***15** 1873

[2] U. Pal and P. Santiago, 2005 *J. Phys. Chem.* B **109** 15317

[3] L. Vayssieres, 2003 *Adv. Mater.* **15** 464

[4] L. Vayssieres, K. Keis, A. Hagfeldt and S. E. Lindquist 2001 *Chem. Mater.* **13** 4395

[5] G. Marci, V. Augugliaro, M. J. Lopez-Munoz, C. Martin, L. Palmisano, V. Rives, M. Schiavello, R. J. D. Tilley and A. M. Venezia, 2001 *J. Phys. Chem.* B **105** 1026

[6] Z. K. Tang, G. K. L. Wong, P. Yu, M. Kawasaki, A. Ohtomo and H. Koinuma, *Appl. Phys. Lett.* **72**, 3270 (1998).

[7] S. Shionoya and W. M. Yen, Phosphor Handbook (CRC Press, Boca Raton, 1999), p. 255.

[8] B. O'Regan and M. Gratzel, **Nature 353**, 737 (1991).

[9] A. V. Dijken, E. A. Mulenkamp, D. Vanmaekelbergh and A. Meijerink, *J. Lumin.* **90**, 123 (2000)

[10] F. Claus, J. Thomas, R. Cees . R and S. Peter. J., *Advanced functional materials* **13**, pp.101-107, 2003.

[11] Nanomaterials: Synthesis, Properties and Applications. Edited by A S Edelstein and R.C.Cammarata 1998.

[12] B. R. Ratna, A. D. Dinsmore et al, The 5th Inter. Conf. on the Sci. and Tech. of display phosphor, November 8-10, 295, 1999.

[13] H. Weller, *Adv. Mater.* 5 (1993) 88

[14] R. J. Lanf and W.D. Bond 1984 *Am. Ceram. Soc. Bull.* **63** 278

[15] H. R. Fallah, M. Ghasemi, A. Hassanzadeh and H. Steki, *Physica B* **373** (2006), p. 274.

[16] S. Sakohara, M. Ishida and M. A. Anderson, *J. Am. Chem.* B, 1998, **102**, 10169

[17] M. Abdulah, T. Morimoto, K. Okuyama, Adv. *Funct. Mater.* **13** 2003 1-5

[18] O. M. Ntwaeaborwa and P. H. Holloway, *Nanotechnology* **16** (2005) 865 -868.

[19] S. M. Haile, D. W. Johnson and G. H. Wiseman, 1989 *J. Am.Ceram. Soc.* **72** 2004

[20] L. E. Brus, *Nanostruct. Matter*, 1992, 1, 71

[21] L. E. Brus, *J. Chem. Phys.*, 1983, 79, 5566.

[22] Z. Zhang *et al* 2006 *J. Phys. Chem.* B **110** 8566

[23] Y. Ni *et al Nanotechnology* **18** (2007) 155603

[24] G. E. Malashkevich, I. M. Melichenko, Poddenezhny, et al., *J. Non-Cryst. Solids,* **260** (1999) 141.

Chapter 5

Structural, thermal and optical properties of ZnO, $SiO_2:Ce^{3+}$ and ZnO: $SiO_2:Ce^{3+}$ nanoparticles by sol-gel process.

5.1 Introduction

Glasses are an important class of optical materials for several reasons; e.g. large samples can be made. Since glasses are amorphous, impurities such as transition metals or rare-earth (RE) elements, incorporated in glasses have broad absorption bands compared to crystal hosts so there is a high efficiency of absorption from broad band sources. Traditionally, glasses are made by heating starting materials past their melting points and then quickly cooling them, causing them to harden into glass. Solution-gelation (sol-gel) method offers a low-temperature alternative for making these materials. Sol-gel silicate glasses are silicate glass monoliths made by the sol-gel process using silicate precursors. Silicon alkoxides is hydrolyzed by water to form a gel at ambient conditions. Slow heating of the gel over a period of 2 weeks causes the gel matrix to collapse. The potential advantages of the sol-gel technique over the traditional melt-and-quench method are the following:

1. The sol-gel process allows materials to be made at low temperature (typically at about 90-100^{0}C). At this temperature, biological and organic impurities can be incorporated into materials.
2. Dopants, which normally come in the form of inorganic salts, can be incorporated easily as solutions. Glasses made by the sol-gel method have the potential to hold higher dopant concentrations than melt glasses, which are critical if they were to be used as materials for laser applications. Melt glasses lose their amorphous structure once the doping levels reach about 0.5 atm % while sol-gel glasses can maintain their amorphous structure even at doping concentrations as high as 10 atm % (1).
3. The sol-gel technique potentially produces higher quality glasses because the quality of starting precursors can be controlled.

4. The sol-gel method allows versatility in shapes and sizes of final products: xerogels, thin films, fiber, etc.

   Sol-gel glasses are of current interest because of their potential applications such as electronics and optics [2]. Applications of sol-gel chemistry can be found in a wide range of areas: films used in plasma display panels [3], optical planar waveguides [4], and thin films sensors [5], etc. Recently, there has been much interest in encapsulating enzymes in sol-gel to study their properties and use them as biocatalysts (6). Since fluorescence in the visible region of the spectrum, RE-doped sol-gel glasses have the potential to be used as solid-state laser materials. Unfortunately, quantum yields of RE-doped sol-gel glasses are typically low compared to those of crystals and melt glasses because of several fluorescence quenching mechanisms.

5.2 Experimental

5.2.1 ZnO synthesised in $SiO_2:Ce^{3+}$ host

ZnO nanoparticles was synthesised using the method explained in section 4.2. To prepare $SiO_2:Ce^{3+}$ sample 20.8g of tetraethylorthosilicate (TEOS) solution was mixed with 9.2g of ethanol and 9.0g of 0.15M HNO_3 as a catalyst . 0.432g of Ce (NO3).$6H_2O$ was dissolved in 9.2g of ethanol then added to the TEOS solution and stirred for 1 hour. The transparent solution was mixed with the ethanol suspension of ZnO nanoparticles (prepared as explained in section 4.2 in the molar ratio 20:1(Si: Zn^{2+}). The yellow mixture formed stiff gel after stirring for 2 days and dried at room temperature for another 6 days.

SOL-GEL PREPARATION OF ZnO:SiO2:Ce

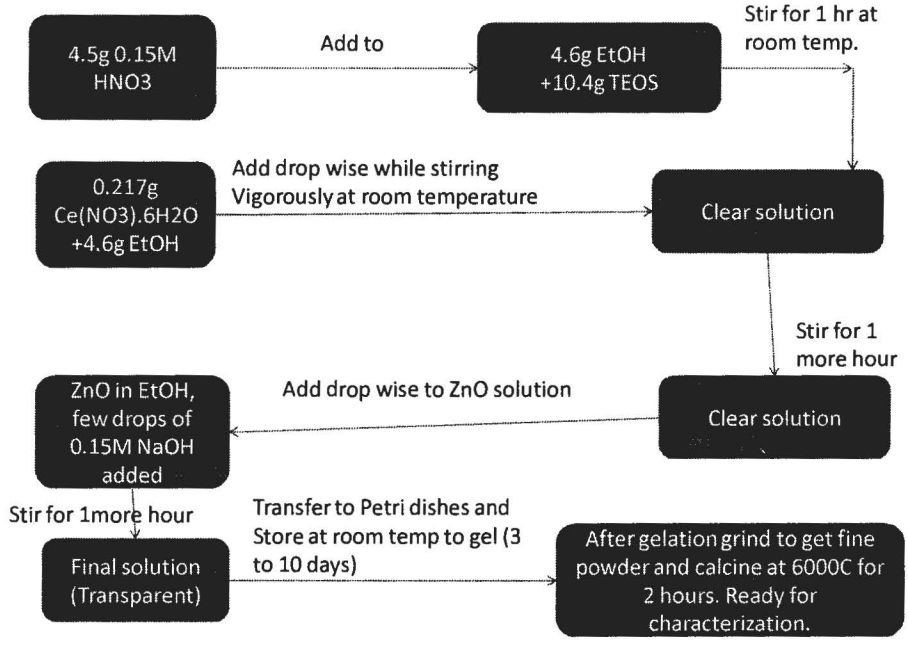

$$Si(OCH2CH3)4 + 2H2O = SiO2 + C2H5OH$$

Figure.5.1. SOL-GEL PREPARATION OF $ZnO:SiO_2:Ce$.

5.2.2 Characterization of the samples.

The X-ray diffraction (XRD) patterns were recorded to characterize the phase and crystal structure of the nanoparticles using a multi-purpose XRD system with Siemens Diffractometer D5000 with a Cu K_α radiation source at 40 kV, 30 mA and λ = 1.5418 Å. The morphology of the nanoparticles was observed by a Shimadzu Superscan SSX-550 system scanning electron microscope (SEM) operated at 200 kV equipped with energy dispersive X-ray spectroscopy (EDS). Optical absorption was performed on an Agilent HP1100 diode-array UV-visible spectrophotometer. Room temperature photoluminescence (PL) of the samples was measured, using a He–Cd laser (325 nm) as excitation sources.

5.3 Results and discussion

5.3.1 X-Ray Diffraction spectrum

Fig. 5.2 below shows XRD pattern from (a) SiO_2 and (b) SiO_2:Ce^{3+} matrices respectively. XRD data from ZnO-SiO_2:Ce^{3+} powders did not show any detectable peaks from ZnO. This could be due to size-broadened ZnO diffraction peaks and high amorphous scattering background from SiO_2 matrix. ZnO particles remained small in the matrix as suggested by lack of diffraction peaks. Using Scherer's equation, the average ZnO nanoparticles diameter obtained was 6nm. It also suggests that the ZnO nanoparticles were well dispersed in the SiO_2 matrix.

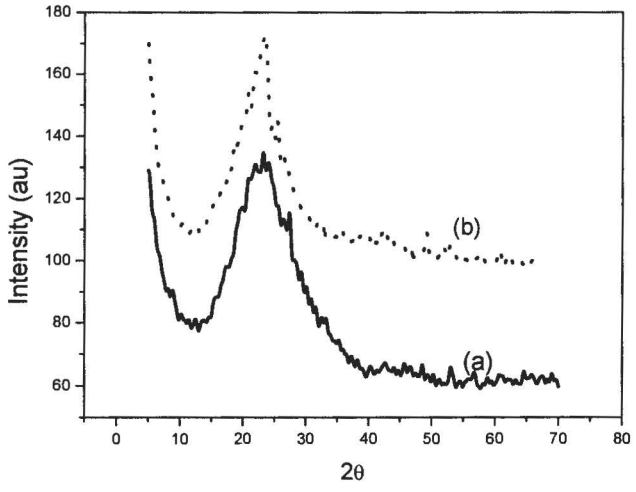

Figure 5.2 Amorphous nature of (a) SiO_2 and (b) ZnO-SiO_2:Ce^{3+}.

5.3.2 Morphological and compositional analysis

The morphology and size of the dried ZnO nanoparticles were examined by SEM observations. A representative SEM image of ZnO powder dried at ambient conditions in a fume cabinet for 2 days is presented in Fig. 5.3(a-d). The presence of some bigger particles should be attributed to the aggregating or overlapping of smaller particles. However, small irregular nano sized particles which are the building block of the large particles are clearly evident as shown by Fig. 5.3(a-d). EDS spectra (Fig. 5.3(f)) were

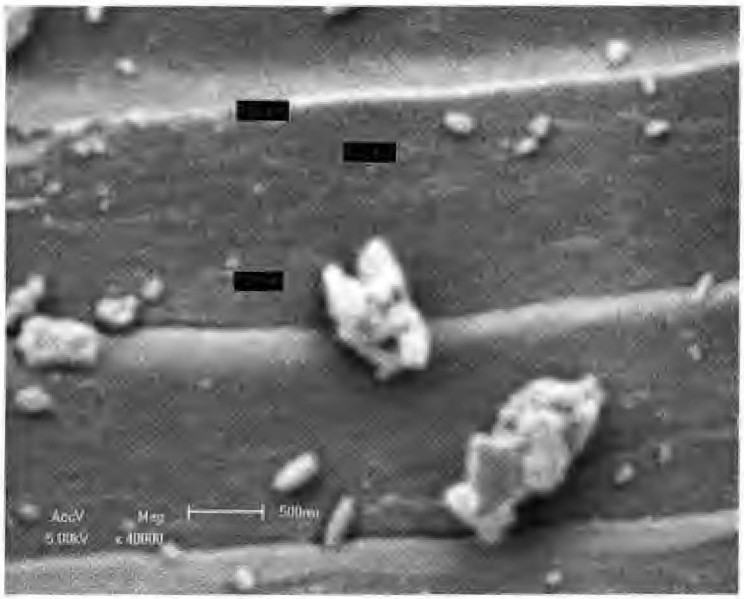

Figure 5.3(a) SiO_2 pure x40000. Showing spherical nanoparticles of about 100nm and bigger agglomerated particles.

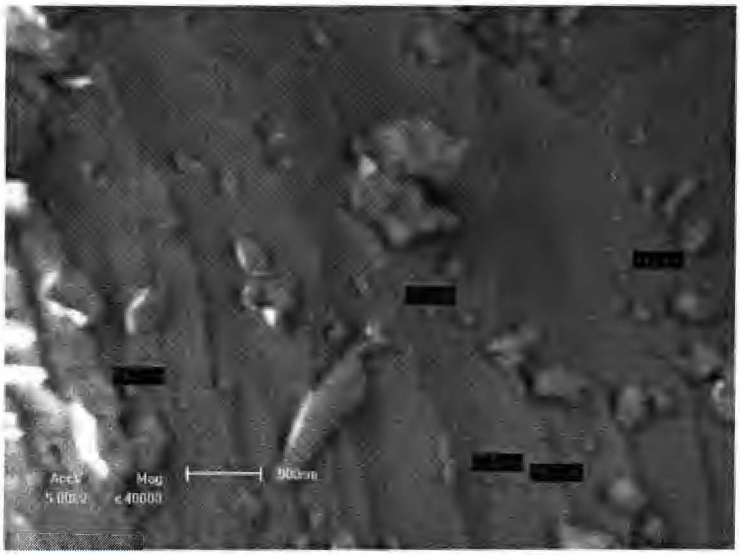

Figure 5.3(b) ZnO-SiO_2:Ce^{3+} (0.22NaOH) x40000. SEM image revealing nanoparticles of diameter between 40nm and 70nm.

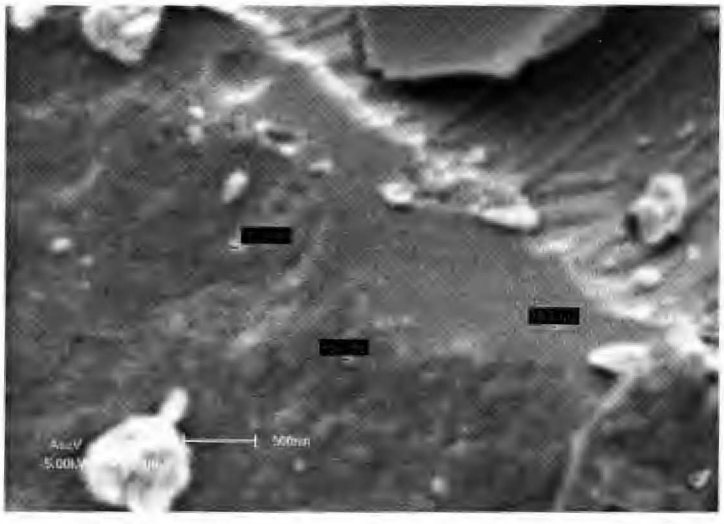

Figure 5.3(c) ZnO-SiO_2:Ce^{3+} (0.33NaOH) x40000. SEM image is similar to that in Fig. (b). Concentration of NaOH seems not to affect particle sizes.

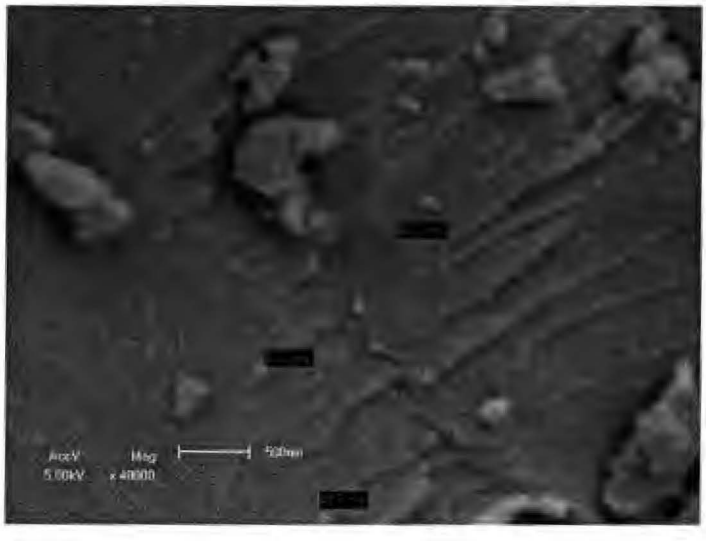

Figure 5.3(d) ZnO-SiO2:Ce^{3+} (0.44NaOH) x40000. Average particle sizes are similar as observed in the above images.

taken for ZnO-SiO_2:Ce^{3+} matrices which were dried for 2 days in air. All expected elements were detected and the adventitious carbon and gold are also to be seen. A low peak of Ce was noted due its low concentration while the Zn peak was quite conspicuous.

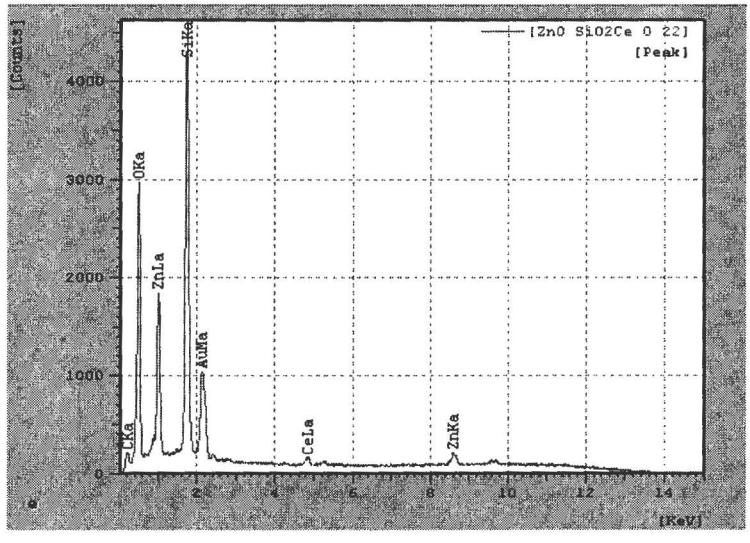

Figure.5.3 (e). EDS of ZnO-SiO_2: Ce^{3+}.

5.3.3 Photoluminescence properties

Fig.5.4 (a) shows the luminescence pattern of pure Silica and 0.5 % Ce^{3+}- doped silica treated at ambient condition in a fume chamber for 2 days. Various researchers have mentioned several luminescence peaks at 450, 560 and 650 nm for pure SiO_2, which is associated with intrinsic defects originating from neutral oxygen vacancies, per oxygen linkages and non bridging oxygen radicals respectively [21]. However, we observed luminescence peaks at 413, 448, 469 and 544 nm for SiO_2. These peaks are slightly blue shifted may be due to the size of the nanoparticles and hence an indication of quantum confinement. Some researchers have attributed the blue shift in SiO_2 to electron-hole recombination between the oxygen vacancies and O_2 linkages [18].

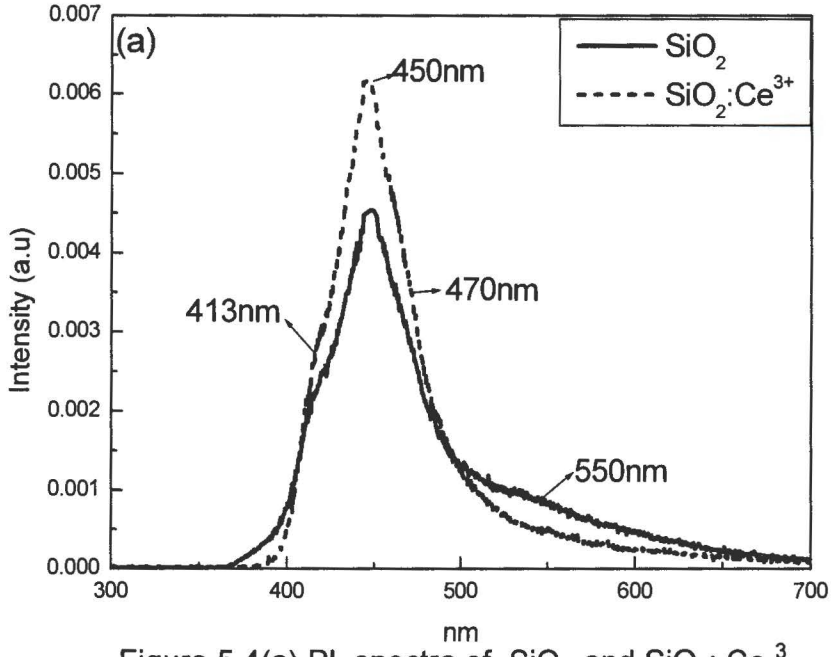

Figure 5.4(a) PL spectra of SiO_2 and SiO_2: Ce^{3}

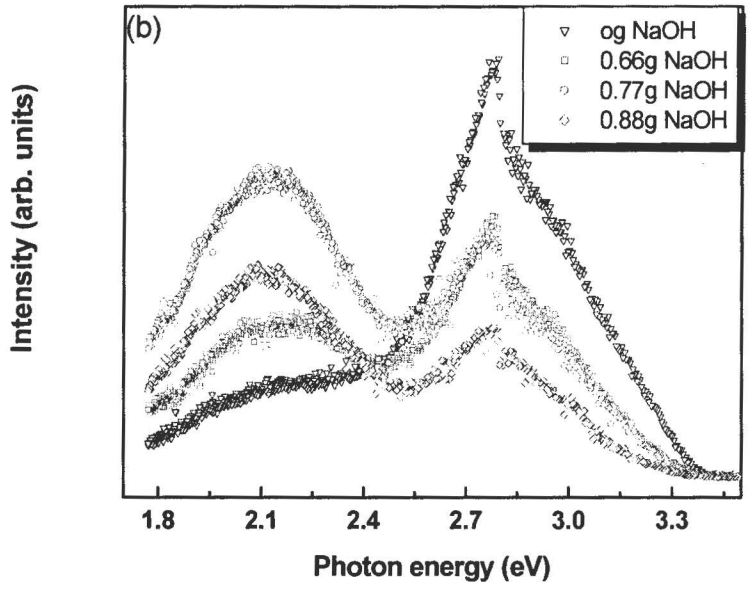

Figure 5.4(b) PL spectra of ZnO: SiO_2: Ce^{3+} composite.

Two main luminescence bands of Ce^{3+} ions at 357 and 450 nm in samples of Ce^{3+} - doped glasses and crystals have been reported [22-24]. Our PL emission spectra from SiO_2: Ce^{3+} is very similar to that of pure silica but with enhanced luminescence. The PL emission at 450 nm could be due to transition in both SiO_2 and Ce^{3+} emitting centres. This implies that there is possibility of host SiO_2 transfers energy to the emitting centre Ce^{3+} just like in the commercially used ZnS: Ag^+, in which the sulphide host transfers energy to Ag^+. The emission from SiO_2 at 550 nm appears to have been quenched in case of SiO_2: Ce^{3+}. Fig. 5.4(b) shows the photoluminescence (PL) spectra of SiO_2 and ZnO-SiO_2: Ce^{3+} powders made using different concentration of NaOH. The emission is mainly in the green and blue region with main peaks at 582, 447 and 413 nm. Incorporation of ZnO clearly leads to increased luminescence for all observed SiO_2: Ce^{3+} peaks. This is despite lower Ce^{3+} emission centers' concentration of 1% of ZnO added. On the contrary it is interesting to observe that at higher concentration of NaOH the broad green emission is enhanced proportionally. Since the emissions of ZnO-SiO_2:Ce^{3+} nanocomposites are similar to those of SiO_2:Ce^{3+}, it may be concluded that it's the sensitization effect of Zn-O-Si interphase that leads to energy transfer from the ground states of Ce^{3+} to its excited states [25-27]. This implies that there has been non radiative energy transfer from the Zn-O-Si interface to Ce^{3+} emission centers. Therefore it appears that nanostructural ZnO sufficiently affected rare-earth ions in glass just like nanometer-sized metal particles [5]. One of the most important requirements of a luminescent material is a high light output and it is imperative that the radiative processes have a much higher probability than the non-radiative ones. However since it is impossible to exclude nonradiative processes, the alternative is to have non-radiative processes that favour a high output through feeding of the luminescent activator and/or population of the emitting level. Since the emissions of ZnO-SiO_2:Ce^{3+} nanocomposites are similar to those of SiO_2:Ce^{3+}, it may be concluded that it's the sensitization effect of Zn-O-Si interphase that leads to energy transfer from the ground states of Ce^{3+} to its excited states. The transfer may be attributed to phonon mediated processes and/or resonance. The photo generated electron from the ZnO are trapped in the band gap defects and since these defect states lie next to Ce^{3+} excited states, energy is nonradiatively transferred to cerium ions.

5.4 Conclusion

In summary, high quality luminescent ZnO powder with different sizes was prepared by wet chemical synthesis through a sol gel process just by adjusting the molar ratio of sodium hydroxide to zinc acetate. XRD confirmed the wurtzite structure of ZnO. All elements expected in the nanoparticles were observed through EDX. SEM showed agglomerated particles albeit with nanosized agglomerates on the surface and which were interpreted as the building particles of the bigger ones. A further indication to nanosized particles of the ZnO powder was revealed by the TEM image and blue shifted luminescence of both UV-vis and PL measurements. The deep level defect emission luminescence is predominant for the prepared ZnO nanoparticles by sol-gel, while the intensity of the green emission luminescence is optimum for OH^-/Zn^+ molar ratio of 4.4. This enhanced luminescence was attributed to quantum confinement caused by the nano sized ZnO nanoparticles. The choice of appropriate molar ratio of the precursor is paramount in the size control of ZnO nanoparticles as no catalyst is employed. At low concentration of NaOH the incorporation of ZnO into SiO_2: Ce resulted in quenching of green emission from ZnO nanopartcles while enhancing blue photoluminescence from the Ce^{3+} activator. This enhanced luminescence was attributed to an energy transfer from the ZnO nanoparticles to the Ce^{3+} activator. In contrast it was noted that at higher NaOH concentrations both the green emission peak of ZnO and blue emission of the activator were enhanced.

References

[1] J. Joo, S. G. Kwon, J. H. Yu and T. Hyeon 2005 *Adv. Mater.***15** 1873

[2] U. Pal and P. Santiago 2005 *J. Phys. Chem.* B **109** 15317

[3] L. Vayssieres 2003 *Adv. Mater.* **15** 464

[4] L. Vayssieres, K. Keis, A. Hagfeldt and S .E. Lindquist 2001 *Chem. Mater.* **13** 4395

[5] G. Marci, V. Augugliaro, M. J. Lopez-Munoz, C .Martin, L. Palmisano, V. Rives, M. Schiavello, R. J. D .Tilley and A. M. Venezia 2001 *J. Phys. Chem.* B **105** 1026

[6] Z. K. Tang, G. K. L. Wong, P. Yu, M. Kawasaki, A. Ohtomo and H. Koinuma, *Appl. Phys. Lett.* **72**, 3270 (1998).

[7] S. Shionoya and W. M. Yen, Phosphor Handbook (CRC Press, Boca Raton, 1999), p. 255.

[8] B. O'Regan and M. Gratzel, **Nature 353**, 737 (1991).

[9] A. V. Dijken, E. A. Mulenkamp, D. Vanmaekelbergh and A. Meijerink, *J. Lumin.* **90**, 123 (2000)

[10] Claus Feldmann, Thomas Justell, Cees R. Ronda, and Peter J. Schmidt, Advanced *functional materials* **13**, pp.101-107, 2003.

[11] Nanomaterials: Synthesis, Properties and Applications. Edited by A .S. Edelstein and R. C. Cammarata 1998.

[12] B. R. Ratna, A. D. Dinsmore et al, The 5th Inter. Conf. on the Sci. and Tech. of display phosphor. November 8-10, 295, 1999.

[13] H. Weller, Adv. Mater. 5 (1993) 88

[14] R. J. Lanf and W. D. Bond 1984 *Am. Ceram. Soc. Bull.* **63** 278

[15] E. Ivers-Tiffee and K. Seitz 1987 *Am. Ceram. Soc. Bull.* **66** 1384 5

[16] H. R. Fallah, M. Ghasemi, A. Hassanzadeh and H. Steki, *Physica B* **373** (2006), p. 274.

[17] S. Sakohara, M. Ishida and M. A. Anderson, *J. Am. Chem.* B, 1998, **102**, 10169

[18] M. Abdulah, T. Morimoto, K. Okuyama *Adv. Funct. Mater.* **13** 2003 1-5

[19] O. M. Ntwaeaborwa and P. H. Holloway *Nanotechnology* **16** (2005) 865 -868.

[20] S. M. Haile, D. W. Johnson and G. H. Wiseman 1989 *J. Am.Ceram. Soc.* **72** 2004

[21] Y. Ni *et al Nanotechnology* **18** (2007) 155603

[22] A. Vab Dijken, E. A .Meuhenkamp, D. Vanmaekelbergh and A.Meijerrink, 2000 *J.*

Lumin. **90** 123

[23] Z. Li, Y Xiong and Y. Xie, 2003 *J. Inorg. Chem* **42** 8105.

[24] K. Tanimura, C. Itoh and N. Itoh *J. Phys. C: Solid State Phys.* **21** 1869-1876 (1988).

[25] G. E. Malashkevich, I. M. Melichenko, Poddenezhny, et al., *J. Non-Cryst. Solids* **260** (1999) 141.

[26] H. Bi, W. Cai and L. Zhang, *Mater. Res. Bul.* **35** (2000) 1495.

[27] V. P. Dotsenko, I. V. Berezozskaya, N. P. Efryushina, et. al., *J. Lumin.* **93** (2001) 137

Chapter 6

Effect of Mn doping on the structural and optical properties of sol-gel derived ZnO nanoparticles

6.1 Introduction

Zinc oxide nanostructures are semiconducting inorganic nanocrystallites with dimensions less than 100 nm, in all three dimensions. Consequently, discrete electronic states, unusual structural transformations, unique optical properties and a blue shift of the band edge transition energy are induced in these nanoparticles [1, 2]. Due to high surface-to-volume ratio, the surface atoms play a large role in the properties of nanomaterials, which usually have fewer adjacent coordinate atoms and can be treated as defects as compared with the bulk atoms. These defects induce additional electronic states in the band gap, which can mix with the intrinsic states to a substantial extent and which may influence the spacing of the energy levels and the optical properties of nanopowders. Thus, nanoparticles especially quantum dots (QDs) exhibit unique properties and have a broad range of applications in optoelectronics, telecommunications, lasers and optical sensors [3,4,5]. Therefore, simple synthesis routes for ZnO nanoparticles with a diameter less than or comparable to QDs which is 7nm for zinc oxide are extremely important in materials research. ZnO is an important commonly n-type wide-energy-gap semiconductor (Eg = 3.37 eV, 330 K) which has a wide range of applications such as in solid-state gas sensors, transparent conducting electrodes, and optical electronic devices [6 - 10]. Among various methods, sol–gel is well suited for production of nanostructured materials, because of its relatively low processing cost and the ability to control the grain size. Although the sol-gel technique has been widely used for the preparation of zinc oxide powders, the potential of this technique to prepare nanomaterials has not been fully explored. In this section, a simple sol-gel route for synthesizing of wide-dispersed ZnO nanostructures within a small diameter range 6 to 20 nm. The novelty of this work is the use of small mole % of Mn ions as do-pants which lead to fabrication of different shapes and structures of ZnO: Mn nanostructures without using of any surfactant or other additives. Doping Mn into ZnO

offers an interesting way to alter various properties [11, 12], for example the band gap of host material can be tuned from 3.37eV to 3.70eV. Also it alters the emission properties by providing an efficient channel for the recombination of electron and hole via the do-pant Mn d levels. By varying the size of particles below 10nm, optical and electronic properties can further be tuned. It is also found that ZnO: Mn exhibit ferromagnetic properties at room temperature [13].

6.2 Experimental details

Colloidal solution was prepared from Zinc acetate and absolute ethanol. 0.918g of Zinc acetate was dissolved in 60mls of absolute ethanol (99.999%) and vigorously stirred for 30 minutes at 80 ^{0}C. Different mole fractions of manganese acetate was dissolved in 10 mls of absolute ethanol and added drop wise to Zn^{2+} solution under vigorous magnetic stirring. 0.55g NaoH was separately dissolved in 20 mls of similar ethanol and stirred in a preheated ultrasonic bath for one hour. This was slowly added to the solution while stirring in ice-water. Stirring ran for 24 hrs and a brownish colloidal solution was washed in a mixture of ethanol and heptane repeatedly. It was then kept in a fume chamber for 2 days to dry.

6.3 RESULTS AND DISCUSSION

6.3.1 Morphological and structural properties

Surface morphological studies of the undoped and Mn-doped ZnO have been carried out using scanning electron micrographs Shimadzu model ZU SSX-550 Super scan coupled with an energy dispersive X-ray spectrometer (EDS). Fig.6.1 shows the SEM images of undoped and Mn-doped ZnO powders. SEM photograph (fig.6.1. a) of pure ZnO shows large, agglomerated and spherical nanoparticles. The Mn (2.5%) doped ZnO was to have wrinkle network surface morphology (Fig. 6.1(b). The formation of many long nanosize rods all over the surface are attributed to the presence of Mn ions. The Mn atoms may have disturbed the growth process by acting as a seed, resulting in the formation of nanosize rods. The decrease in manganese concentrations seems to

increase the radii and the lengths of the cylindrical nanorods formed as shown by figures (Fig. 6.1(c)) and (Fig. 6.1(d)). Therefore the incorporation of Mn at Zn site was found to influence the surface morphology of the powders. It is interesting to note that the grain sizes observed from SEM is significantly different from the grain size determined from using XRD measurements. This shows the grains seen in the SEM are the domains formed by aggregation of nanosize crystallites [15].

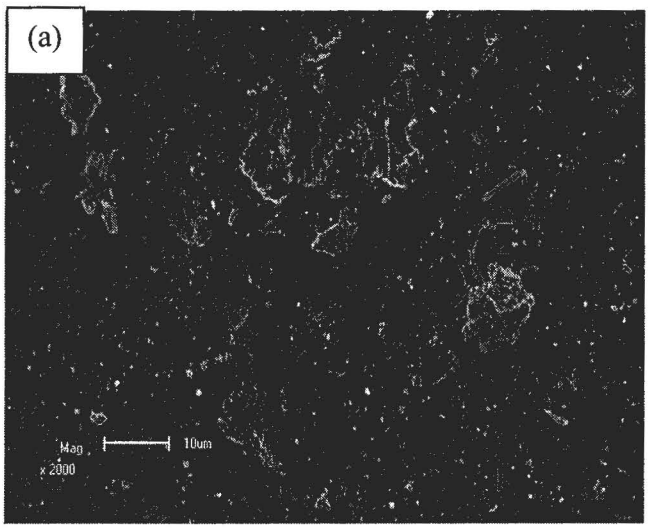

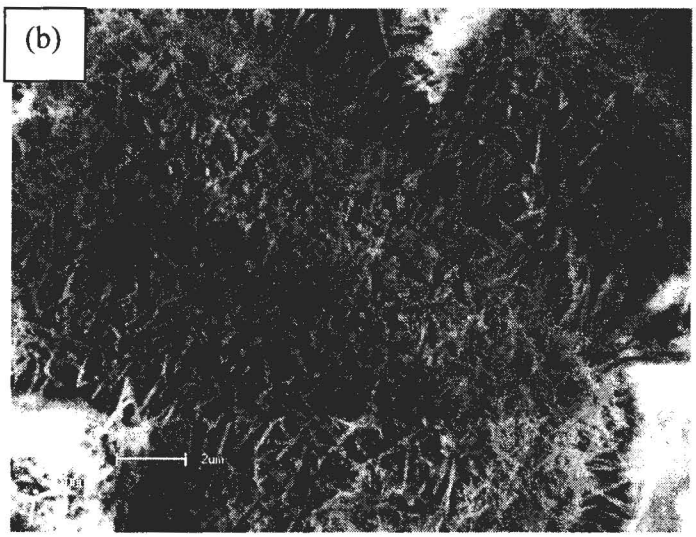

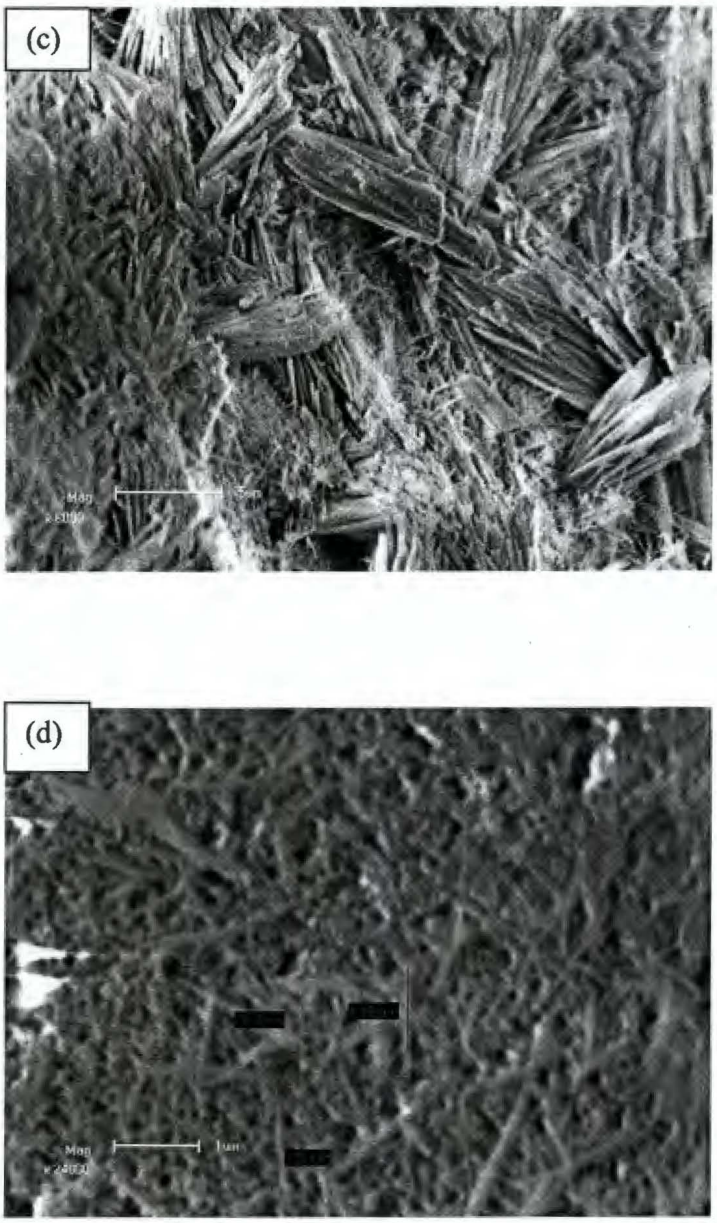

Figure 6.1 SEM micrograph of (a) undoped ZnO nanoparticles, (b) ZnO: Mn 2.5% nanorods with wrinkled network, (c) ZnO: Mn 2% nanorods with log-like intertwined network, and (d) ZnO: Mn 1.5% with wrinkled network.

Fig. 6.1(a) shows SEM image of undoped ZnO nanoparticles with spherical shapes. The estimated nanoparticles sizes are in the range of 80 to 100nm. The large and agglomerated particles are domains formed by aggregation of nanosize crystallites.

Fig. 6.1(b) Indicate SEM image obtained when ZnO was doped with 2.5%Mn. Nanorods with wrinkled network with estimated lengths and diameter of 10 micrometers and 2 micrometer respectively, were obtained all over the surface. This could be due to that fact that Mn atoms acting like seeds may have interfered with the growth process forming ZnO nanorods.

Fig. 6.1(c) and (d) show thicker (4 to 8μm) nanorod images in the form of intertwined networks. Reduction in the concentration of Mn in ZnO seems to increase the thickness of the nanorods. This increase of the diameters of the nanorods at lower Mn concentrations could be attributed to less interference to the growth process of the ZnO nanorods by Mn atoms as compared to SEM image in Fig. 6.1(b) with higher Mn concentration. Energy dispersive x-ray analysis showed that the amount of Mn element in the sample increased depending on the increasing Mn incorporation in the solution. As a result, Mn incorporation has a strong effect on the optical, structural and morphological properties of ZnO. The Energy dispersive x-ray spectra shown in Fig. 6.2 consists of Zn and O and confirms the presence of manganese in the ZnO particles with wt % are less than the nominal value of Mn in ZnO (Note: traces of C less than 0.1 wt % are also observed). Manganese is different from other transition metals when substituted in an $A^{II}B^{VI}$ matrix, since it forms stable phases over a wide range of compositions. It appears that the ease with which the manganese substitutes for the group II elements in the zinc-blende and wurtzite structures results from the fact that the 3d orbitals of Mn are exactly half-filled. Fig. 6.1(a) is representative of XRD patterns taken from the pure and Mn doped ZnO nanoparticles prepared by sol-gel technique. The superior structural properties of the reference nanostructures are clearly reflected by the XRD results. In general, these particles were characterized by sharp, well-defined peaks with no preferred orientation. . Strongly pronounced peaks, <100>, <002> and <101> appear at 2 theta = 31.43, 34.13 and 35.93 respectively, which indicate that the samples are polycrystalline. Few weaker peaks can also be seen in Mn-doped sample in the XRD pattern. These few peaks may be assigned to Mn_3O_4.

That is to say, not all the stoichiometric Mn^{2+} has entered the ZnO lattice, the rest of Mn^{2+} has been oxidized into manganese oxide.

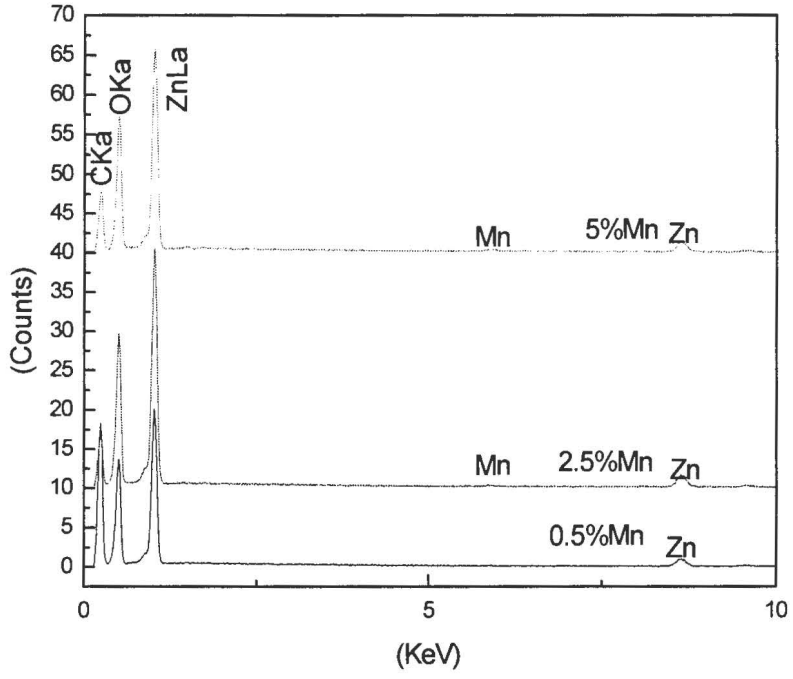

Figure 6.2 EDS analysis.

Ivill et al. [15] has also reported the precipitation of Mn_3O_4 in $Zn_{1-x}Mn_xO$ powder deposited on sapphire by pulsed laser deposition (PLD) at the Mn concentration of 3 at %. Samples were randomly orientated along different planes, the "d" value were compared with standard JCPDS data card (79-0207) which confirms the wurtzite structure of the materials. Crystallite size of the ZnO powder samples was calculated from the peaks width using Debye- Scherer formula;

$D = (0.9\lambda) / (\beta_{1/2} \cos\theta)$,

Where, D is the diameter of the crystallites, λ is the wavelength of Cu K_α line, and β is full width at half maximum (FWHM).

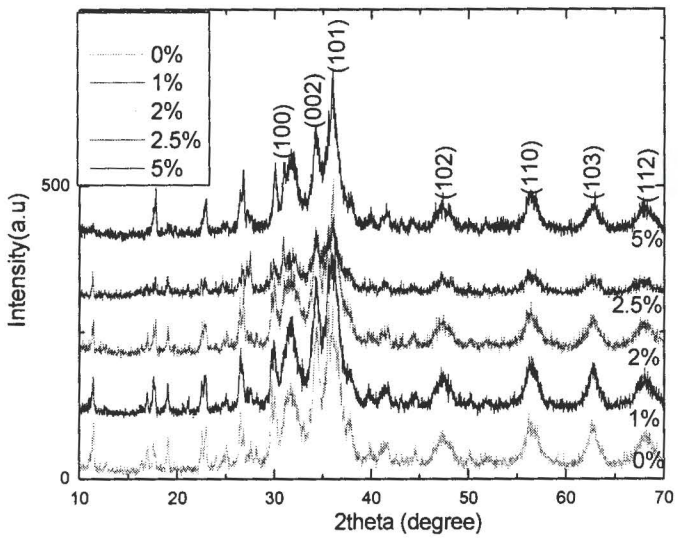

Figure 6.3(a) XRD pattern of ZnO: Mn with various concentration of mn^{2+}.

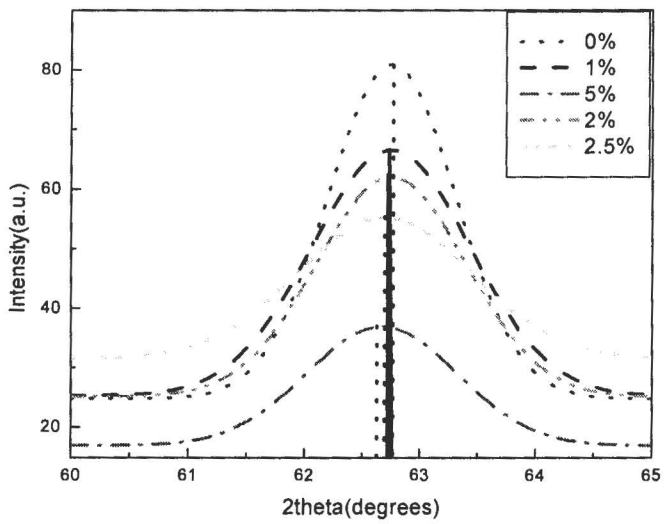

Figure 6.3 (b). XRD spectra of doped and undoped ZnO powders at single plane, i.e. <110>.

The calculated particle sizes of pure and Mn doped samples were obtained in the range of 5- 7nm as tabulated in Table.6. 1.

Table 6.1 Average particle size as a function of mol% Mn^{2+}.

Average grain size as function of mol% Mn^{2+} in ZnO					
Sample	<102>	<110>	<103>	<112>	average grain size (nm)
ZnO	6.7	7.0	7.0	6.6	6.8
ZnO:Mn1%	6.1	7.0	7.0	6.2	6.6
ZnO:Mn2%	5.4	6.8	6.9	5.9	6.3
ZnO:Mn2.5%	5.2	6.4	6.9	5.7	6.1
ZnO:Mn5%	5.9	7.4	7.1	5.6	6.5

The peaks (especially high angle peaks) of the diffraction patterns of doped samples are slightly shifted to lower angles with increase in Mn molar ratio (see Fig. 6.3. (b)). Fig. 6.3(c) Shows an approximately linear relation between the <110> peak position and the amount of mol % of Mn^{2+} ions present in the sample. This means that small variation in the lattice parameters occur as Mn^{2+} concentration in the sample increases. The lattice constants of Mn doped ZnO obtained by least square method, shown in Table 6.2 were slightly larger than those of undoped ZnO, because the ionic radius of Mn (II) (0.66) is larger than that of Zn (II) (0.60) [11]. The length of both *a* and *c* axis expand slightly with the increasing Mn^{2+} doping in ZnO. The expansion of the lattice constants (table 6.2) and the slight shift of XRD peaks with an increase in concentration of Mn doped ZnO indicated that manganese has really doped into the ZnO structure.

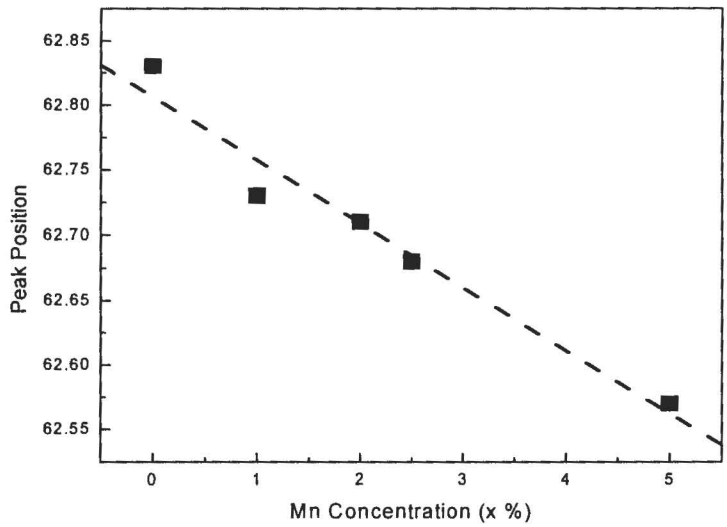

Figure 6.3(c) Variation of <112> peak position with Mn mole % concentrations.

Table 6.2 Lattice constants of pure and Mn-doped ZnO nanoparticles.

Sample	Lattice parameter		
	a	c	c/a
ZnO	3.246	5.208	1.604
ZnO:Mn1%	3.265	5.221	1.599
ZnO:Mn2%	3.270	5.237	1.601
ZnO:Mn5%	3.279	5.245	1.599

The average ratio *c/a* of Mn-doped ZnO is approximately 1.600, which is slightly less than that of pure ZnO (1.604). This value is related to the positional '*u*' parameter in the wurtzite structure and the Zn–O bond length *l* is calculated using the '*u*' parameter. The Zn–O bond lengths calculated for pure ZnO and Mn-doped ZnO powders from FTIR measurements are 1.9758 and 1.9762 Å, respectively. The interplanar spacing has been increased due to a slight shift in 2θ for the Mn-doped powder, which is consistent with Zn–O length. Substitution of Mn^{2+} for Zn^{2+} requires a local expansion of the lattice to accommodate the manganese ion due to ionic radii difference. This induces higher

covalent bonding for the Mn^{2+} substitutes in ZnO: Mn, which is in agreement with the bond length determined.

6.3.2 Optical properties

6.3.2.1 Transmission and Absorbance

Optical absorption spectra of the undoped and Mn- doped ZnO powder recorded in the wavelength region of 200–850nm is shown in Fig 6.4. The absorbance is found to be minimum for undoped ZnO powder sample and increases with an increase in mole Mn%. The decrease in optical absorption is associated with the loss of light due to (i) oxygen vacancies and (ii) scattering at grain boundaries. A characteristic difference in the absorption edge was observed with Mn incorporation in ZnO. A sharp absorption edge has been observed for undoped ZnO while Mn-doped display slightly lesser sharp drop in absorption edge. This implies slight difference in size distribution of the monodispersed nature of the nanoparticles between pure and doped samples.

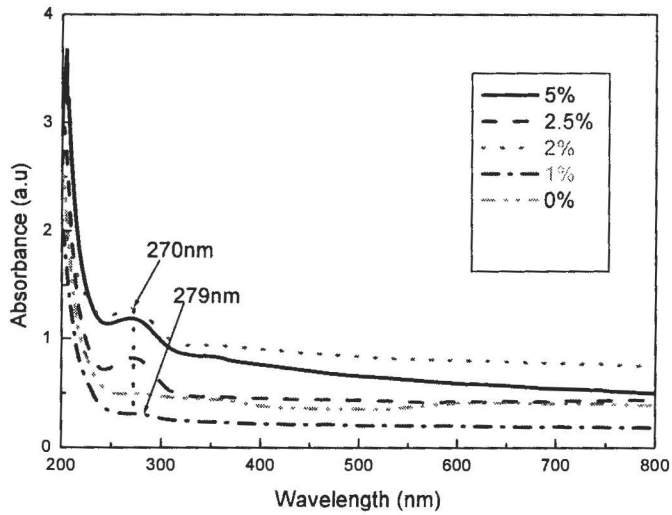

Figure 6.4 (a) UV-vis absorption spectra of undoped and doped ZnO nanoparticles

It is clearly visible from absorbance spectra that the excitonic absorption peak shift towards the lower wavelength side with the Mn-doped ZnO nanoparticles. This values lie much below the band gap wavelength of 375 nm (E_g = 3.3) of bulk ZnO [15]. The relatively high absorbance at longer wavelengths and broad absorption edge for doped ZnO indicates large dispersion in size of the ZnO: Mn nanostructures and their arbitrary orientations. The position of the absorption band is observed to shift towards the lower wavelength side with the Mn-doped ZnO nanoparticles.

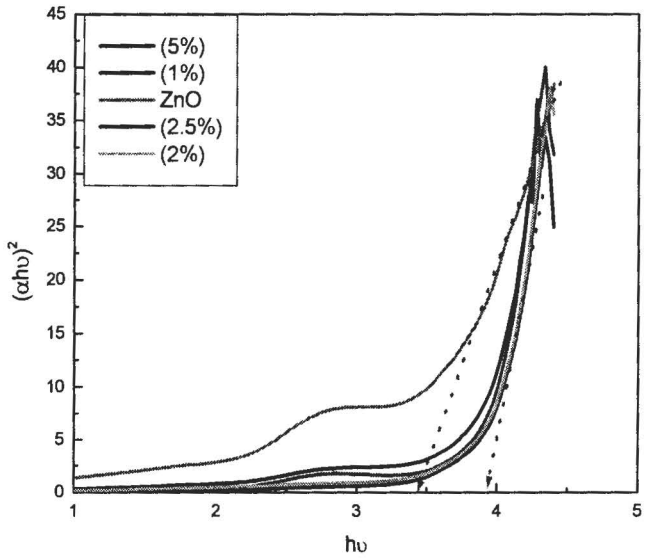

Figure 6.4 (b) Graph of $(\alpha h\upsilon)^2$ vs.$h\upsilon$ for different concentrations of Mn in ZnO. Mn

This confirms the XRD findings that the band gap of ZnO material changes with the doping concentration of Mn^{2+} ion. Similar observation of enhancement of the band gap of ZnO with Mn^{2+} ion concentration was also made earlier by Mandal and Nath and Fukumura et al. [16, 17]. The increase in band gap from bulk ZnO with dopant concentration (x) can be attributed to the sp–d spin exchange interaction between the band electrons and localized spin of the transition metal ions [17]. It is clear that the ZnO nanoparticles doped with Mn have an excellent absorbing UV ray capability. The relationship between the optical absorption coefficient (α) and the incident photon

energy (hu) from the optical absorption measurements for a direct band-gap material is given by;

$$(\alpha h\upsilon)^2 \sim (h\upsilon - Eg) \quad (1)$$

Using this information, graphs of $(\alpha h\upsilon)^2$ were plotted against hu and the linear region was extrapolated to $(\alpha h\upsilon)^2 = 0$ to give a value of the optical energy gap. The experimental optical band gap values for layers with varying manganese content (i.e. x = 0, 1, 2, 2.5 and 5 mol %) were found to be approximately 3.43, 3.84, 3.88, 3.92 and 3.84 eV as tabulated in Table 6.3. Fig. 6.4 displays the band-gap variation of the ZnO: Mn nanostructures as a function of manganese concentrations. It can also be seen from Fig. 6.3 that band gap value slightly increases to approximately 3.92 eV with an increase in Mn concentration but for Mn molar of 5% correlation does not hold, this could imply that Mn ions are not fully incorporated into ZnO lattices.

Table 6.3. Average particle size as a function of mol% Mn^{2+}.

Sample	Band Gap (eV)
ZnO	3.43
ZnO:1%	3.84
ZnO:2%	3.88
ZnO:2.5%	3.92
ZnO:5%	3.84

6.3.2.2 Photoluminescence properties

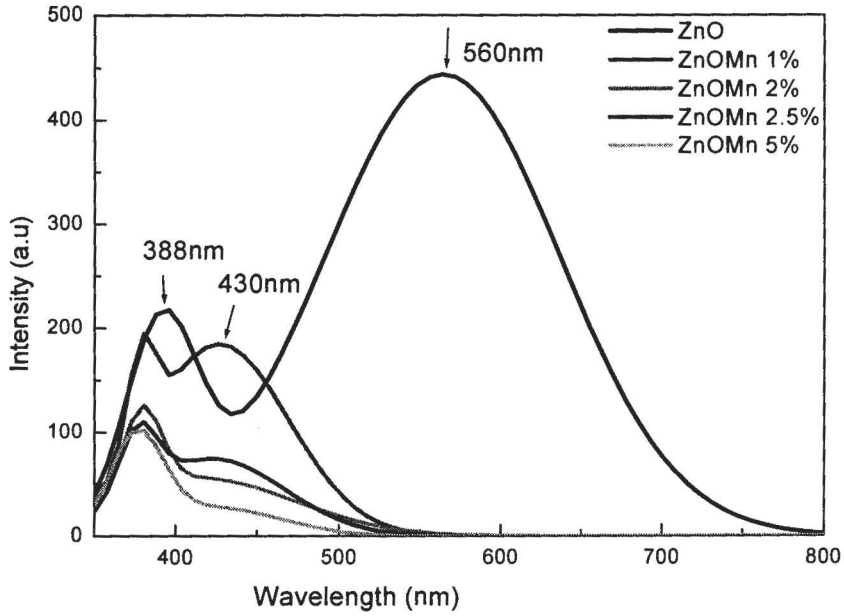

Figure 6.5 Fluorescence spectra (obtained with λext =325nm) of ZnO and Mn-doped ZnO with various concentration of Mn.

Comparison of the fluorescence spectra of the doped and the undoped samples exhibits two spectral features at 388nm and 560nm common to most of the samples. The feature at 388nm corresponds to the near-band-gap emission, and the broad feature at 560nm has been attributed to surface traps. These emissions found to be extremely broad may be due to phonon assisted by transition. On doping with Mn, we observe that the surface traps are significantly quenched, as indicated by a marked reduction of emission feature at 560nm. The reduction in the surface traps is attributed to quenching of the surface traps by the doped Mn ions. The 1 % Mn sample displayed luminescence intensity at 430nm completely different from all other samples. This is possibly due to the emission from the Mn ions. It is clear from the graph that doping of ZnO with Mn quenches significantly the green emission and slightly the yellow one. Liu et al observed similar results when they investigated the green and yellow luminescence in Mn- doped

ZnO which was attributed to interstitials Zn and oxygen. Surface defects plays an active role in the ZnO quantum dots which have OH^- radical on its surface responsible for quenching green luminescence. For ZnO particles doped with Mn^{2+} an increase in the Mn^{2+} emission was observed with an increase in manganese concentrations. This was explained by more efficient trappings of electron-hole pairs by Mn^{2+} in smaller ZnO particles as a result of an increased wave function overlap. For a long time one region of green luminescence has been attributed to the defect levels arising either due to oxygen vacancies or due to Zinc interstitials.

6.4 Conclusion

We have synthesized high purity nanorods of ZnO and ZnO: Mn having micrometer-sized lengths in the laboratory using sol-gel technique. SEM images gave good results of synthesized nanorods. XRD patterns confirm the polycrystalline wurtzite structure of ZnO. Both the green and blue emission in ZnO was quenched when doped with Mn^{2+}. Mn doped nanorods have several applications as the best suited materials for sensors, spintronics, high energy density batteries, better insulation materials etc. Photoluminescence spectra of the undoped ZnO are composed of two main emission bands peaked at 388 nm and 560 nm. Doping ZnO with Mn^{2+} quenches both of these bands. At room temperature, the super-radiation phenomena of the UV photoluminescence seems to be produced at only high density excitation, therefore the UV emissions are ascribed to intrinsic exciton photoluminescence. However, green band probably originates from the defect related to oxygen.

References

[1] F. C. M. Van De Pol *Ceram. Bull.* 69, 1959, 1990.

[2] K. Nashimoto, S. Nakamura and H. Mariyama *Japan. J. Appl. Phys.* 43 5091, 1995.

[3] T. Nagata, T. Shimura, A. Asida, N. Fujimura and T. Ito *J. Cryst. Growth* 237,537, 2002.

[4] A. J. Freeman, K. R. Paeppelmeier, T. O. Mason, R. P. H. Chang and T. J. Marks *Mater. Res. Soc.* Bull. 25 45,2000.

[5] L . Spanhel, M. A. Anderson, *J.Am.Chem. Soc.*, 113, 2826, 1991.

[6] X. Wu, A. Yamilov, X. Liu, S. Li, V. P. Dravid, R. P. H. Chang and H. Cao, *Appl Phys Lett* **85** (2004), p. 3657.

[7] N. F. Cooray, K. Kushiya, A. Fujimaki, D. Okumura, M. Sato, M. Ooshita and O. Yamase, *Jpn J Appl Phys* **38** (1999), p. 6213.

[8] Y. J. Xing, Z. H. Xi, Z. Q. Xue, X. D. Zhang, J. H. Song, R. M. Wang, J. Xu, Y. Song, S.L. Zhang and D.P. Yu, *Appl Phys Lett* **83** (2003), p. 1689.

[9] W. Shan, W. Walukiewicz, J. W. Ager, K. M. Yu, Y. Zhang, S. S. Mao, R. Kling, C. Kirchner and A. Waa, *Appl Phys Lett* **86** (2005), p. 153117.

[10] Z. W. Jin, Y. Z. Yoo, T. Sekiguchi, T. Chikyow, H. Ofuchi, Fujioka, M. Oshima, H. Koinuma, Appl. Phys. Lett. 83 (2003) 39.

[11] H. J. Lee, S. Y. Jeong, C. R. Cho, C. H. Park, Appl. Phys. Lett. 81(2002) 4020.

[12] G. Srinivasan, J. Kumar, Cryst. Res. Technol. 41 (2006) 893.

[13] C. J. Murphy, *Appl. Spec.* **56**, 16A, 2002.

[14] M. Ivill, S. J. Pearton, D. P. Norton, J.Appl. Phys.97 (2005) 053904.

[15] S. Sakohara, M. Ishida and M. A. Anderson, *J. Am. Chem.* B, 1998, **102**, 10169

[16] T. Fukumura, Z. Jin, M. Kawasaki, T. Shono, T. Hasegawa, S. Koshihara, H. Koinuma, Appl. Phys. Lett. **78**, 958 (2001).

[17] S. K. Mandal, T. K. Nath, Thin Solid Films 515(2006) 253

Chapter 7

7.1 Conclusion

This thesis report that high quality luminescent ZnO powder with different particle sizes was prepared by sol-gel process by adjusting the molar ratio of sodium hydroxide to zinc acetate. XRD results confirmed the polycrystalline wurtzite structure of ZnO and revealed particles sizes of about 7nm. All expected elements were present in the nanoparticles as observed through EDS. SEM showed agglomerated particles albeit with nanosized agglomerates on the surface and which were interpreted as the building particles of the bigger ones. A further indication to nanosized particles of the ZnO powder was revealed by the TEM image and blue shifted luminescence of both UV-vis and PL measurements. The deep level defect emission luminescence is predominant for the prepared ZnO nanoparticles by sol-gel, while the intensity of the green emission luminescence is optimum for OH^-/Zn^+ molar ratio of 4.4. This enhanced luminescence was attributed to quantum confinement caused by the nano sized ZnO nanoparticles. The choice of appropriate molar ratio of the precursor is paramount in the size control of ZnO nanoparticles as no catalyst is employed. At low concentration of NaOH, the incorporation of ZnO into SiO_2: Ce resulted in quenching of the normal green emission from ZnO nanopartcles while enhancing blue photoluminescence from the Ce^{3+} activator. This enhanced luminescence was attributed to an energy transfer from the ZnO nanoparticles to the Ce^{3+} activator. In contrast it was noted that at higher NaOH concentrations both the green emission peak of ZnO and blue emission of the activator were enhanced. High optical transmittance greater than 80% was achieved in the visible spectral wavelengths with UV-Vis optical absorption and transmission measurements.

For Zinc oxide doped manganese(ZnO: Mn) samples synthesized using similar technique high purity nanorods of ZnO having micrometer-sized lengths were revealed by SEM. XRD patterns confirm the polycrystalline wurtzite structure of ZnO. Both the green and blue emission in ZnO was quenched when doped with Mn^{2+}. Mn doped nanorods have several applications as the best suited materials for sensors, spintronics, high energy density batteries, better insulation materials etc. Photoluminescence spectra of the undoped ZnO are composed of two main emission bands peaked at 388

nm and 560 nm. Doping ZnO with Mn^{2+} quenches both of these bands. At room temperature, the super-radiation phenomena of the UV photoluminescence seems to be produced at only high density excitation, therefore the UV emissions are ascribed to intrinsic exciton photoluminescence. However, green band probably originates from the defect related to oxygen.

Future work

The following are possible future work in the same area of research;

1. Doping ZnO with Mn and Co-doping with Al.
2. Doping of ZnO with rare-earth elements e.g. Eu, Tb, Pr, Dy etc.
   Characterization techniques will be similar to the ones in this work.